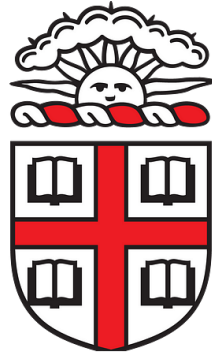


A Computational and Experimental Investigation of Twisted Trilayer Graphene

Brown University Department of Physics



Submitted in partial fulfillment of the Honors requirements for the
Bachelor of Science in Mathematical Physics.

Anvita Bhagavathula

May 2023

Abstract

Twisted trilayer graphene is a unique 2D moiré system that exhibits exotic properties such as superconductivity at certain temperatures, twist angles, electric displacements, and magnetic fields. The focus of this thesis is to investigate whether we can take a quantum mechanical first-principles approach to understand the electronic interactions of this system, with the ultimate goal of shedding more light on the nature of the superconducting phase. I will use Density Functional Theory (DFT), an *ab-initio* modeling technique, as the first-principles framework to examine the electronic structure of our system of interest. DFT was chosen because of its ability to capture all of the electronic interactions in a system. In parallel, experimentally, I will fabricate this system in the lab to measure its transport and phase properties to carry out a side-by-side comparison to computational predictions. I will present preliminary results, highlighting the parameters and computational setup to carry our first-principles calculations. This includes a user-interactive Python program called **TriCrystal** to generate computational twisted trilayer graphene structures, and band structures of AB-stacked bernal bilayer graphene and a twisted trilayer graphene system with a twist angle of 21.79° . Lastly, I will discuss the challenges faced by the chosen first-principles approach, specifically in regards to carrying out calculations for large moiré superlattices that correspond to the experimental twist angle range of interest. Given the scope of the thesis, I will propose potential solutions to address these challenges, which will be the focus of future efforts.

Acknowledgements

First, I want to thank Professor Jia Li for helping me pursue this project and bridge my experimental learnings with theory. In a field where it is easy for individuals such as myself to feel demoralised and isolated, I am lucky to have been supported by someone who has encouraged me to be ambitious and explore my passions from the very beginning. Thank you for believing in me.

I also want to thank Professor Brenda Rubenstein for being open to this project and for providing me with her time and energy throughout the process. Learning from her wealth of knowledge on the subject has strongly reinforced my love for science.

I want to thank Tilas Kabengele, a graduate student in the Rubenstein group, for his endless patience, support, and mentorship on the computational side of the project. Thank you for always being willing to answer my emails and address my questions. I have learnt so much, both about research and life, by collaborating with you.

This thesis would also not have been possible without the wonderful community I was lucky to be a part of through the Li Lab at Brown. Thank you Gene, Derek, Xiaoxue, Erin, Lin, James, Yusra, Yibang, Changye, and Sara, for your support throughout the experimental side of the project. Thank you for staying up with me at night to stack and answering every single question I have. You have taught me the importance of having community and compassion in the pursuit of science.

To my friends - Grace, Luke, Zoe, Joe, Rachel, Meher and Momoka - who have stood by me through everything for the last four years, your belief in me is what motivates me everyday; you are my family.

Lastly, to my *amma* and *nanna*, Sujatha and Ravi, and my grandparents - thank you for always encouraging me to be curious about the world. Your strength, unconditional love, and support of my dreams is what has made this thesis possible. Thank you for teaching me how rewarding studying the universe could be.

Contents

1	Introduction	1
2	Theoretical Background	3
2.1	Electronic Structure of Solids	3
2.1.1	Band Structure	3
2.2	Experimental Summary of Multilayer Graphene Systems	5
2.2.1	Graphene	6
2.2.2	Twisted Bilayer Graphene	7
2.2.3	Twisted Trilayer Graphene	8
2.3	Kohn-Sham Density Functional Theory	9
2.3.1	The Kohn-Sham Equations	10
2.3.2	Exchange, Correlation, and Dispersion	13
2.3.3	The DFT Algorithm	15
2.4	Density Functional Theory for Periodic Solids	17
2.4.1	Periodic Boundary Conditions	17
2.4.2	Plane Waves and Bloch's Theorem	17
2.4.3	Pseudopotentials	18
2.4.4	Brillouin Zone Sampling	19
2.5	Advantages and Limitations of DFT	19
3	Computational Methods	20
3.1	The TriCrystal Code	20
3.1.1	Algorithm and Usage	20
3.1.2	Example Structure Visualisation	24
3.2	Converging Structural Parameters	26
3.3	Generating Band Structure	29

4 Experimental Methods	30
4.1 Flake Exfoliation	30
4.1.1 The “Scotch-Tape” Method	30
4.1.2 Silicon Wafer Cleaning	30
4.1.3 Graphite	31
4.1.4 Boron Nitride	31
4.1.5 Cataloguing and Optical Microscopy	31
4.2 Atomic Force Microscopy	32
4.2.1 Thickness Estimation	32
4.2.2 Cutting and Lithography	33
4.3 Device Stacking	33
4.3.1 PPC and PC Preparation	33
4.3.2 Device Assembly Through Transfer Station	35
4.4 Circuit Design	39
4.5 Electron Beam Lithography and Fabrication	39
5 Discussion	44
5.1 Preliminary Results	44
5.2 Further Work	47
5.3 Summary of Thesis Achievements	48

Chapter 1

Introduction

The objective of this thesis is to investigate the electronic properties of a unique 2D moiré system, twisted trilayer graphene, from two distinct angles: computational and experimental. A 2D moiré system is formed by layering periodic lattices on top of one another and introducing a relative twist angle between the two layers. This twist angle causes a mismatch in the periodicity of the layers, resulting in a large-scale interference pattern, known as a moiré superlattice [20] (See Figure 1.1). Physical moiré systems created by stacking various monolayer materials on top of one another have been found to have exotic electronic and phase properties. Moiré systems made from graphene have been found to have a host of interesting properties such as alternating insulating and superconducting states at varying charge carrier concentrations.

The superconducting phase is highly intriguing owing to its versatile tunability and potentially unconventional order parameter structure [32]. While extensive experimental efforts have been devoted to investigate the nature of this phase, it remains an outstanding challenge to directly probe the nature of its electronic interactions and explore their role in stabilizing superconductivity. The focus of this thesis will be to investigate whether we can take a quantum mechanical first-principles approach to understand the electronic interactions present within the moiré flat energy band in twisted trilayer graphene, with the ultimate goal of shedding more light on the nature of pairing instability of the superconducting phase. I will use Density Functional Theory (DFT), an *ab-initio* modeling technique, as the first-principles framework to examine the electronic structure of our system of interest. In parallel, experimentally, I will fabricate this system in the lab to measure its transport and phase properties to carry out a side-by-side comparison to computational predictions.

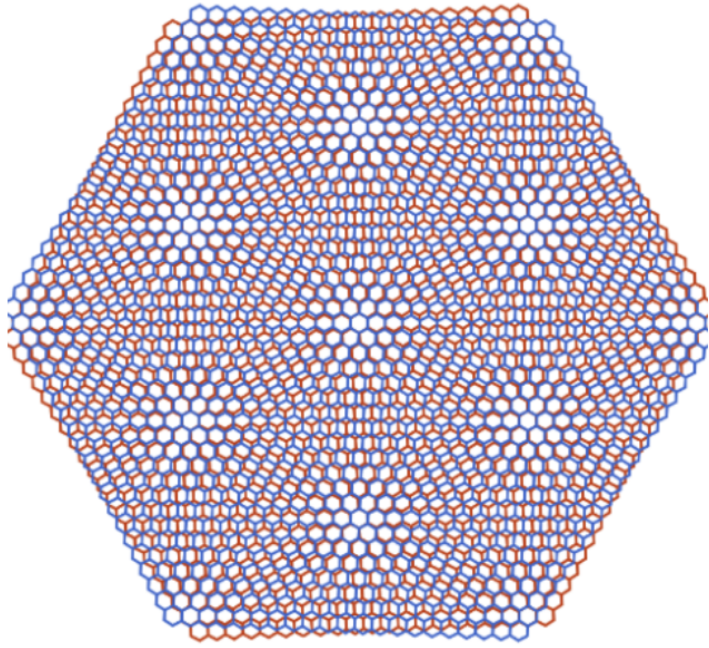


Figure 1.1: A 2D Moiré superlattice of twisted bilayer graphene generated by stacking two monolayer pieces of graphene on top of one another with a relative twist angle. The large-scale interference pattern is known as a moiré pattern. [29].

DFT was chosen because of its ability to capture all of the electronic interactions in a system. I will present preliminary results, highlighting the parameters and computational setup to carry these first-principles calculations. This includes the development of a user-interactive Python program to generate computational twisted trilayer graphene structures, and the generation of band structures of AB-stacked bernal bilayer graphene and a twisted trilayer graphene system with a twist angle of 21.79° . Lastly, I will discuss the challenges faced by the chosen first-principles approach, specifically in regards to carrying out calculations for large moiré superlattices that correspond to the experimental twist angle range of interest. Given the scope of the thesis, I will propose potential solutions to address these challenges, which will be the focus of future research efforts.

Chapter 2

Theoretical Background

2.1 Electronic Structure of Solids

The electronic structure of a physical system refers to its electron configuration. Specifically, where its electrons reside in its orbitals and their associated energies [11]. There are several ways to analyse the electronic structure of a system but we will focus on one such framework for understanding electronic structure: the band structure picture of electrons.

2.1.1 Band Structure

The electronic band structure picture of a solid illustrates how electrons in the solid arrange themselves in allowed energy bands [22]. Specifically, it describes the energy levels that electrons can occupy within that solid. Additionally, this picture also highlights forbidden energy regions where no electrons can exist; these are known as band gaps [22]. Let us treat a solid system as a periodic crystal lattice. The energy bands of this system are obtained by solving the single-particle Schrödinger equation for an electron in a periodic potential. Specifically, we apply the *nearly free electron model* to an electron in this system; this model adds a weak periodic perturbation to the framework of the *free-electron model* and aims to account for the electron-nuclear interactions in a crystal while leaving out complex electron-electron interaction terms [33]. The Hamiltonian of this system H has the form

$$H = \frac{\mathbf{p}^2}{2m} + V(\mathbf{r}) \quad (2.1)$$

where \mathbf{p} is the momentum vector of an electron, m is its mass, and \mathbf{r} is its position. Here, we assume the potential repeats itself

$$V(\mathbf{r}) = V(\mathbf{r} + \mathbf{R}) \quad (2.2)$$

with periodicity \mathbf{R} that corresponds to the periodicity of the crystal lattice. Solving the Schrödinger equation with this periodic potential gives us wavefunction solutions of the form

$$\psi_{\mathbf{k}}^{\alpha}(\mathbf{r}) = e^{i\mathbf{k}\cdot\mathbf{r}} u_{\mathbf{k}}^{\alpha}(\mathbf{r}) \quad (2.3)$$

where \mathbf{k} is known as the crystal momentum and the wavefunctions are indexed using α , which are energy band indices [33]. Another way to motivate our understanding of this picture is to understand what \mathbf{k} physically represents. In a crystal, \mathbf{k} takes values inside the *Brillouin zone*, a type of unit cell defined in reciprocal space. The reciprocal space of a lattice is generated using a Fourier transform of position space [33]. The function $u_{\mathbf{k}}^{\alpha}(\mathbf{r})$ is yet another periodic function. For a given value of \mathbf{k} , we can obtain α solutions to the Schrödinger equation. By calculating these discretized energies for a given band $E_{\alpha}(\mathbf{k})$, we can obtain a dispersion relation for the energies as a function of varying values of the crystal momentum \mathbf{k} . Plots of this dispersion relation are known as the band structure of a system [22].

Another important aspect of band theory is its ability to illustrate the conductivity of a system. There are two families of bands that lie above and below the Fermi energy level of a system known as the conduction and valence bands respectively [3]. The conduction band corresponds to the orbitals where electrons can move freely; this movement is what generates an electric current in the material [3]. The valence band, on the other hand, corresponds to the highest energy filled orbitals of a system. If supplied with enough energy, electrons from the valence band can jump into the conduction bands, allowing the material to conduct electricity [3]. The energy required for this transition to happen, or the energy difference between the lowest conduction band and the highest valence band, is known as the band gap of the material. A larger band gap results in a less conductive material. As shown by Figure 2.1, insulators have a large band gap which prevents their electrons from moving freely in the conduction bands, metals contain overlapping bands which allow these electrons to move freely, and semiconductors have small band gaps

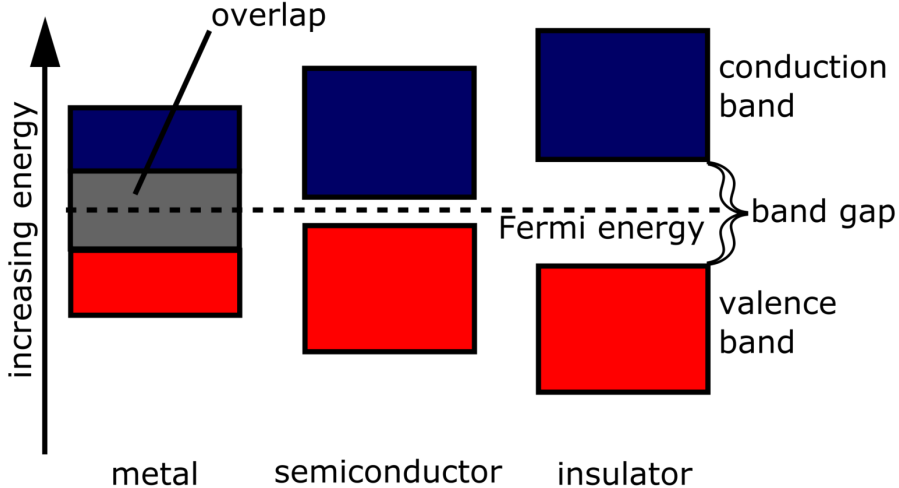


Figure 2.1: An illustration showing how conductivity is related to band gap size. Specifically, we see the band gap structure for a metal conductor, a semiconductor, and an insulator. This figure was adapted from [1].

which allow them to conduct electricity if they are provided with an applied potential [3].

Beyond these conventional band structures, new types of energy dispersions have also emerged. These correspond to novel and exotic physical phenomena. Two such dispersions we will highlight for the purpose of this thesis is the formation of flat bands and Dirac cones [39]. Flat bands are the spectral bands that have momentum-independent energy [4] while Dirac cones represent regions where electrons behave as massless fermions [32]. The relevance of these features becomes especially important in the study of twisted trilayer graphene and will be further discussed in Section 2.2.

2.2 Experimental Summary of Multilayer Graphene Systems

In this section, we motivate why we are interested in studying twisted trilayer graphene. We establish the properties of graphene and its band structure and then discuss recent experimental findings about twisted bilayer graphene and twisted trilayer graphene.

2.2.1 Graphene

Twisted trilayer graphene is made from graphene, a material with unique electronic properties. Graphene is made from carbon atoms arranged in a hexagonal honeycomb lattice where one carbon atom is bonded to three others. It conducts heat and electricity very efficiently and as a result, is used widely for a range of devices such as electronics. Due to its unique chemical bonding, each carbon atom in the system has a free valence electron [13]. These electrons are responsible for graphene's band structure, shown in Figure 2.2, which can be derived by solving the Schrodinger equation with a tight binding Hamiltonian. The band structure consists of Dirac cones, points on the Brillouin zone where linear valence and conduction bands touch at the Fermi energy.

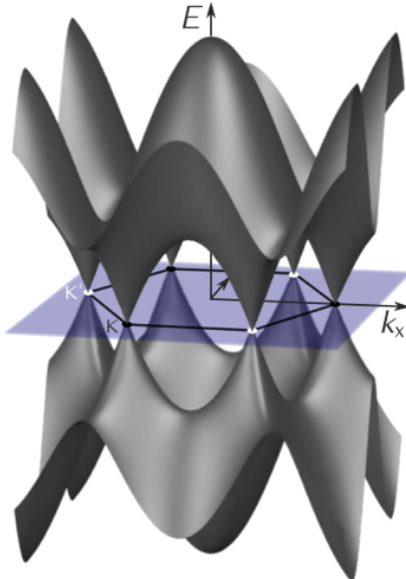


Figure 2.2: The band structure of graphene in the first Brillouin zone [13].

Along the Dirac Cones, the electrons have a linear energy dispersion relation and behave like massless Fermions [13]. Graphene has a twofold valley degeneracy of its Fermi energy, occurring at K and K' on the Brillouin zone, and a twofold spin degeneracy due to the up and down spin orientation of its free electrons [13]. Its band structure gives rise to properties such as high carrier mobility and zero-gap semiconductance. Graphene can also be stacked on top of other 2D materials, including itself, to create stacked systems that exhibit interesting electronic phenomena.

2.2.2 Twisted Bilayer Graphene

The most fundamental system formed from stacking layers of graphene on top of one another is twisted bilayer graphene. This system is constructed by stacking two monolayer graphene layers on top of one another with a relative twist angle θ . This system can be visualised in Figure 2.3 and is a moiré system. We see that this superlattice is composed of two types of stacking arrangements: AA-stacked graphene and AB-stacked graphene. Electron density is strongly concentrated at regions with AA-stacked geometry while it is largely depleted at AB-stacked geometries [5].

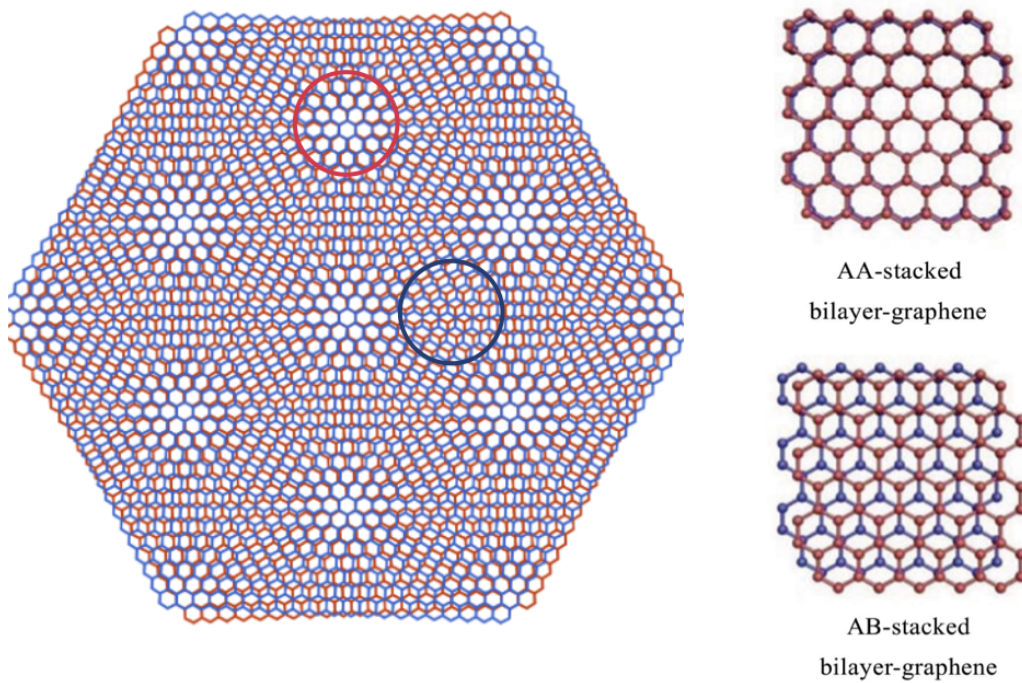


Figure 2.3: Stacking arrangements of graphene in a moiré superlattice of twisted bilayer graphene [17] [29].

In 2018, twisted bilayer graphene with $\theta = 1.1^\circ$ was experimentally found to have coexisting superconducting and correlated insulating phases [6]. Researchers measured the four-probe resistance of this system at varying temperatures and carrier densities, as shown in Figure 2.4, and found that the resistance drastically varied across these parameters. This was unexpected behaviour for such a system. If we examine the band structure of this system, also shown in Figure 2.4, we can attempt to find the origin of this behaviour. We see the formation of unique band structure features, known as flat bands, near the Fermi energy. Flat bands are spectral bands that have momentum-

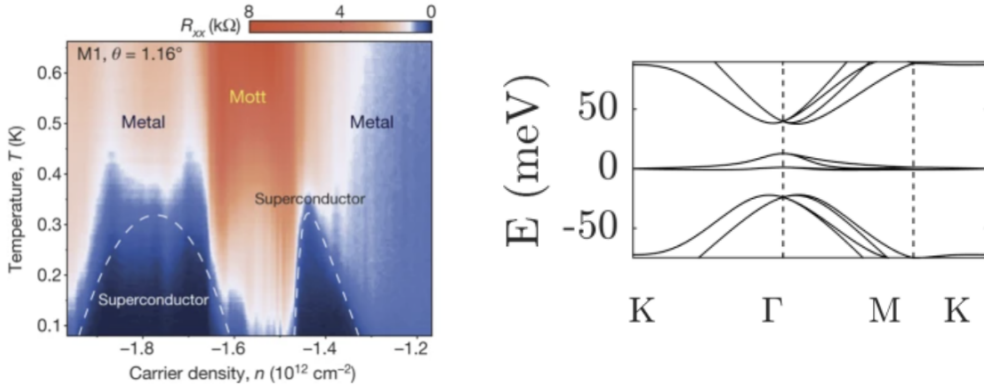


Figure 2.4: The four-probe resistance of twisted bilayer graphene at varying temperatures and carrier densities (left) and the band structure of this system (right) [6][7].

independent energy [4] and the presence of these bands indicates that there is extensive degeneracy of the single-particle electron states [4]. At these regions, underlying theories of solid-state systems with weakly interacting electrons break down [4] [18]. As a result, flat bands are likely explained by novel strongly-correlated phases of matter [4]. In the case of twisted bilayer graphene, these flat bands have been mapped to the correlated insulating phases present in twisted bilayer graphene. In addition to flat bands, we see conical bands above and below the Fermi energy with a twofold degeneracy and an energy gap between them that are reminiscent of the band structure of monolayer graphene.

2.2.3 Twisted Trilayer Graphene

The final 2D moiré system we will discuss is twisted trilayer graphene. This system is constructed using three monolayer graphene layers that have been stacked on top of one another with the middle-layer having been rotated by a twist angle of θ . This structure is shown in Figure 2.5. In 2021, this system was discovered to have tunable superconductivity at a twist angle of $\theta = 1.57^\circ$ [32]. By measuring the four-probe resistance of this device at varying carrier densities and perpendicular electric displacement fields, they generated a rich phase diagram for this device shown in Figure 2.5 [32]. They found varying levels of resistance at different combinations of electric field and carrier densities. While there were zero-resistance regions, there were no insulating phases, only superconducting and conducting ones [32].

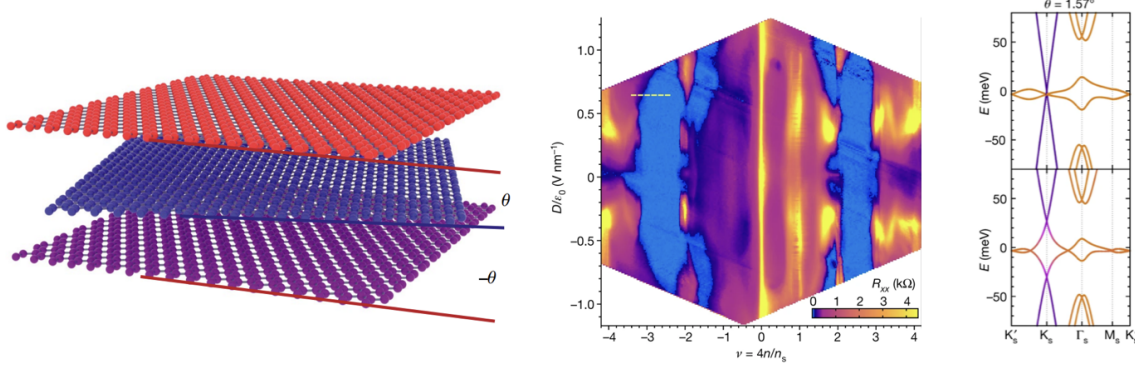


Figure 2.5: The stacked structure of twisted trilayer graphene (left), its four probe resistance measured at varying carrier densities and perpendicular electric displacement fields (middle), and its tight-binding band structure generated for zero displacement field (top-right) and a finite displacement field (bottom-right) [32].

We can also examine this system's band structure, also shown in Figure 2.5, at varying electric displacement fields to further understand the origin of this behaviour. We see the co-existence of Dirac cones that are characteristic of monolayer graphene, with flat bands, features that have been linked to correlated insulating states. At an applied perpendicular electric field, the Dirac Cones are lifted from the charge neutrality point at the Fermi energy and an energy gap between them emerges. Simultaneously, they hybridize with the flat bands, which become more flat [32]. While these are interesting band structure features, they cannot directly be mapped to experimentally observed behaviour. The condensed matter community is still researching the underlying mechanism for this exotic behaviour. One of the key components of gaining a deeper understanding of this mechanism is to have access to a more detailed quantum mechanical picture of the system than the tight binding model, used by experimentalists to generate band structures, can provide. The next section of this thesis introduces a framework to generate this more detailed picture: Density Functional Theory.

2.3 Kohn-Sham Density Functional Theory

Density Functional Theory (DFT) is an ab initio modeling technique that is used to calculate and study the ground-state electronic structure of many-body systems [31]. It can be used to study atoms, molecules, and solids. The fundamental idea behind this method is to reframe the quantum many-body problem as a single-particle one by solving

for the total electron density of a system as opposed to the behavior of its component electrons [38]. DFT was first proposed by Walter Kohn and Pierre Hohenberg in 1964 to study the ground state of an interacting electron gas [16]. Their work demonstrated that the ground-state properties of a many-electron system can be studied using an electron density in three spatial directions [16].

This work was iterated over in 1965 by Kohn and Lu Jeu Sham who defined an energy functional for this electron gas and proved that the ground-state electron density minimizes this functional using the variational principle [16]. DFT became popular shortly after its formulation because of its ability to predict experimental observables for a wide range of systems. It was also much more computationally effective compared to other electronic structure calculation methods such as Møller-Plesset perturbation theory or the Coupled Cluster numerical technique [31]. Its popularity has continued due to the growth in our high-performance computing capabilities and the development of new software to perform calculations. In the following sections, we will discuss the physical formalism underlying this technique.

2.3.1 The Kohn-Sham Equations

The fundamental problem that DFT addresses is solving the many-body Schrodinger equation [15]. Calculating the properties of any given solid material requires us to obtain the system's many-nuclei or many-electron wave function [15]. We can decouple the behaviour of the much larger nuclei by treating them as point-like particles in the Born-Oppenheimer approximation, which states that the motion of the relatively heavier nuclei of a system is fixed while the much lighter electrons are dynamic [14]. As a result, we can treat the wavefunctions of the nuclei and electrons separately. Therefore, we are now interested in determining the wavefunction of a system of N interacting electrons moving in an external Columbic potential [2]. This wavefunction can be obtained by solving the Schrodinger equation using the Hamiltonian \hat{H}

$$\hat{H} = - \sum_{i=1}^N \frac{1}{2} \nabla_i^2 + \sum_i \sum_I \frac{Z_I}{|r_i - R_I|} + \frac{1}{2} \sum_i \sum_{j \neq i} \frac{1}{|r_i - r_j|} + \frac{1}{2} \sum_i \sum_{J \neq I} \frac{Z_I Z_J}{|R_I - R_J|} \quad (2.4)$$

which is a summation of the kinetic energy, the potential energy generated from the field of the positively charged nuclei, and the electron-electron interaction energy

[34]. More specifically, an electron at position r interacts with a nucleus of charge Z at position R with energy $\frac{-Z}{|r-R|}$, two electrons repel one another via the energy $\frac{1}{|r_i-r_j|}$, and two nuclei repel one another with energy $\frac{Z_I Z_J}{|R_I-R_J|}$ [25]. Directly solving this equation is challenging: the wavefunction solutions are complex even for small numbers of N and the required computational power scales rapidly with a larger number of electrons [2].

Density Functional Theory addresses these limitations by analysing 2.4 through the frame of reference of the electron density of the system rather than the electrons[2]. Specifically, Kohn and Hohenberg proposed that the ground state energy of a system of interacting electrons is a functional of its electron density [25]. This reduced the dimensionality of the system from the $3N$ spatial coordinates of the electrons to the 3 spatial coordinates of the electron density, allowing calculations to become computationally feasible even for larger systems. The wavefunction ψ could be expressed using the system's ground state electron density $n_0(\mathbf{r})$.

$$\psi_0(r_1, \dots, r_N) \rightarrow n_0(\mathbf{r}) = \int d^3r_2 \dots d^3r_N |\psi_0(r_1, \dots, r_N)|^2 \quad (2.5)$$

Rewriting 2.4 in terms of the electron density, we obtain a new Hamiltonian \hat{H}

$$\hat{H} = -\sum_{i=1}^N \frac{\nabla_i^2}{2} + \sum_{i=1}^N v(\mathbf{r}_i) + \frac{1}{2} \sum_{i=1}^N \sum_{j=1}^N \frac{1}{|\mathbf{r}_i - \mathbf{r}_j|} \quad (2.6)$$

$$\hat{H} = \hat{T} + \hat{V} + \hat{V}_{ee} \quad (2.7)$$

which is a sum of the kinetic, potential, and electron-electron interaction energies based on the electron density. Building on this fundamental shift in perspective, Kohn and Hohenberg introduced three theorems which enabled them to solve 2.6 [2]:

- **Theorem 1** The system's ground state electron density $n_0(\mathbf{r})$ is what governs the external potential that acts on the system $v(\mathbf{r})$. It hence directly impacts the Hamiltonian, and by extension, the physical properties of the system.
- **Theorem 2** The ground-state energy of the system E_0 can be written as a functional of the electron density $n_0(\mathbf{r})$ using the variational principle. The inequality $E_0[n_0] < E[n]$ is true for all other densities n .

- **Theorem 3** A density-functional $F[n]$ exists such that the ground-state energy functional $E_0[n]$ can be written as $E_0[n] = F[n] + \int d^3r v_0(\mathbf{r})n(\mathbf{r})$. This functional $F[n]$ is independent of the potential $v_0(\mathbf{r})$ and is not unique to a particular system.

Kohn and Sham used these theorems to develop an effective single-particle framework in reference to the electron density. Using this framework, the ground-state energy of the system can now be obtained by finding the self-consistent solution of the following fictitious one-electron Schrödinger equation

$$\left[-\frac{\nabla^2}{2} + v_s(\mathbf{r}) \right] \varphi_i(\mathbf{r}) = \varepsilon_i \varphi_i(\mathbf{r}) \quad (2.8)$$

where the electron density can be found using a set of N orbitals $\varphi_i(\mathbf{r})$, which are all in the ground state

$$n(\mathbf{r}) = \sum_i |\varphi_i(\mathbf{r})|^2 \quad (2.9)$$

and these equations are known as the Kohn-Sham equations [2]. Density Functional Theory aims to solve these equations in a self-consistent manner. Specifically, we want to approximate a fictitious single-particle potential $v_s(\mathbf{r})$ such that the electron-density of the auxiliary noninteracting system described by 2.8 is equivalent to the electron density of the true interacting system [2]. We can work backwards using the energy defined in **Theorem 3** to derive this single-particle potential. Let us first partition the functional $F[n]$ into

$$F[n] = T_s[n] + U[n] + E_{xc}[n] \quad (2.10)$$

where $T_s[n]$ is the total kinetic energy of the non-interacting system [2]. $U[n]$ is the Coulombic electrostatic interaction energy

$$U[n] = \frac{1}{2} \int d^3r \int d^3r' \frac{n(\mathbf{r})n(\mathbf{r}')}{|\mathbf{r} - \mathbf{r}'|} \quad (2.11)$$

and E_{xc} is defined to be the exchange-correlation energy. The exchange-correlation energy can conceptually be thought of as the remaining energy in the system apart from

the non-interacting kinetic and electrostatic terms. It includes complex electron-electron interactions in the system [37]. Mathematically, E_{xc} is given by

$$E_{xc}[n] = T[n] + V_{ee}[n] - U[n] - T_s[n] \quad (2.12)$$

effectively accounting for the remaining interactions within the system [2]. Using these energy definitions, we can solve for the fictitious single-particle potential $v_s(\mathbf{r})$ by applying them to 2.8

$$v_s[n](\mathbf{r}) = v(\mathbf{r}) + \int d^3r' \frac{n(\mathbf{r}')}{|\mathbf{r} - \mathbf{r}'|} + v_{xc}[n](\mathbf{r}) \quad (2.13)$$

where the exchange-correlation potential v_{xc} is defined as the functional derivative of an unknown exchange-correlation energy term

$$v_{xc}[n](\mathbf{r}) = \frac{\partial E_{xc}[n]}{\partial n(\mathbf{r})} \quad (2.14)$$

ultimately establishing that the single-particle potential $v_s(\mathbf{r})$ must be solved using a self-consistent scheme as it is directly dependent on the electron density [2].

2.3.2 Exchange, Correlation, and Dispersion

The Kohn-Sham equations defined in the previous section can be solved using an iterative algorithm. However, prior to delving into the computational method used to solve these equations, we need to discuss some of the practical aspects of carrying out these calculations. Specifically, we will briefly outline how we choose exchange-correlation energy functionals and also how we address dispersion within our system. While we have defined the mathematical form of E_{xc} , this is not sufficient to apply it to practical calculations. Since we do not know its exact form, approximations for this functional are used instead.

Usually, these approximations are system-dependent and can vary across calculations. It has been theorised that the true form of E_{xc} is a universal functional that can be applied to any system [2]. For now, however, we will discuss two distinct approximations that are used to numerically calculate this energy functional. The first is known as a

local density approximation (LDA) and has been popular since the 1970s. In this model, the system is treated as a uniform electron gas where the exchange-correlation energy E_{xc}^{LDA}

$$E_{xc}^{LDA}[n] = \int d^3r n(\mathbf{r}) e_{xc}^{unif}(n(\mathbf{r})) \quad (2.15)$$

is directly dependent on the local electron density at a given point in space [20] [2]. Specifically, $e_{xc}^{unif}(n(\mathbf{r}))$ is the local exchange-correlation energy per particle of this electron gas uniformly distributed in space. This value can be calculated using quantum Monte Carlo methods [2]. The LDA approximation has been widely used for its accuracy across a range of systems. Another commonly used approximation is a generalized gradient approximation (GGA). This new type of approximation tackles the assumption made in LDA approximations that electron density is uniform. This approximation therefore depends on the gradient of the electron density [20]. Specifically, we see that the exchange-correlation energy E_{xc}^{GGA}

$$E_{xc}^{GGA}[n] = \int d^3r F(n(\mathbf{r}), \nabla n(\mathbf{r})) \quad (2.16)$$

is dependent on a function F which in turn is dependent on the gradient of the electron density [2]. The introduction of GGAs have allowed DFT to be a computationally less expensive alternative to other quantum-chemistry modelling techniques, as they have increased its accuracy [2]. We also need to account for other intermolecular forces which arise due to the random motion of electrons around atoms or nuclei. The formation of temporary dipoles when electrons distribute themselves asymmetrically around a nucleus [10] gives rise to attractive forces between dipoles in the system. These are known as London dispersion forces and form a significant part of Van der Waals interactions [10]. Due to their significance in any large physical system, DFT takes them into account when carrying out electronic structure calculations.

There have been several proposed methods to integrate dispersion forces into DFT calculations. The method used in thesis is known as the exchange dipole moment (XDM) dispersion model. The attractive dispersion forces in this model are calculated as interactions between an instantaneous dipole moment in the exchange hole in one molecule and the induced dipole moment in another [9]. By using the dipole moment of an exchange

hole $d_\sigma(\mathbf{r})$

$$d_\sigma(\mathbf{r}) = -\mathbf{r} - \int h_\sigma(\mathbf{r}, \mathbf{r}') \mathbf{r}' d\mathbf{r}' \quad (2.17)$$

where $h_\sigma(\mathbf{r}, \mathbf{r}')$ is known as the exchange-hole wavefunction

$$h_\sigma(\mathbf{r}, \mathbf{r}') = -\frac{1}{n_\sigma(\mathbf{r}_1)} \sum_{i,j} \varphi_{i\sigma}(\mathbf{r}) \varphi_{j\sigma}(\mathbf{r}') \varphi_{j\sigma}(\mathbf{r}) \varphi_{i\sigma}(\mathbf{r}') \quad (2.18)$$

with occupied Kohn-Sham orbitals [20][9]. This wavefunction is calculated numerically by applying the Becke-Roussel model [9]. Using this dipole moment, a Van der Waals energy term is then calculated and added as a correction term after a self-consistent energy calculation has been carried out [9].

2.3.3 The DFT Algorithm

Now that we have established the DFT framework, the significance of exchange-correlation potentials, and Van der Waals corrections, we are in a position to discuss how electron density and system properties are practically calculated in a self-consistent manner. DFT calculations often carry out an iterative algorithm. The first step of this algorithm involves producing an initial guess for the electron density. Next, the energy terms in 2.4 are calculated. Using this approximated energy of the system, the time-independent Schrodinger equation of the form

$$H\psi = E\psi \quad (2.19)$$

is solved again to generate an electron-density dependent wavefunction. Using this wavefunction, a new electron density is then determined using 2.9. At this stage, the energy computed using the previous electron density guess and the new electron density are compared by generating their energy difference. This process is then repeated several times and terminates when the energy difference converges [23]. This is when we obtain converged Kohn-Sham equations, wavefunctions, and energies which are then used to compute several other properties of a physical system such as its band structure and its density of states. A flowchart visualizing this algorithm is provided in Figure 2.6.

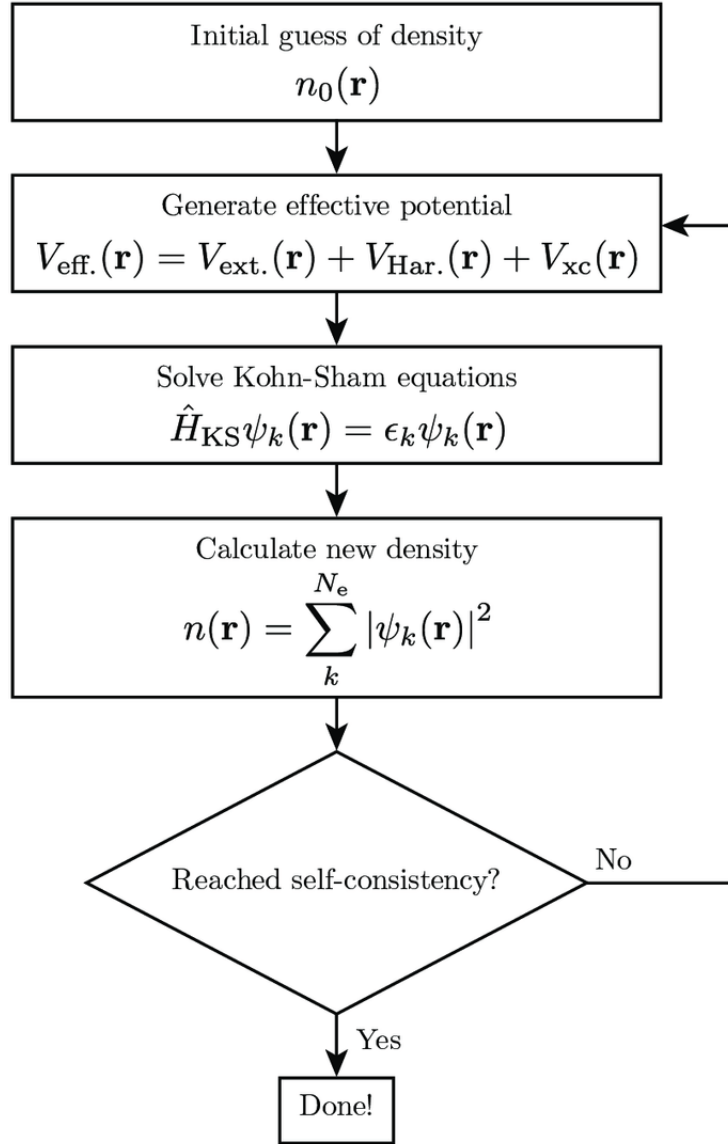


Figure 2.6: A flowchart depicting the iterative algorithm used to carry out DFT calculations. This flowchart was adapted from [35].

2.4 Density Functional Theory for Periodic Solids

So far we have discussed the algorithmic nature of DFT and its underlying theory. However, we need to address how DFT can be practically applied to determine properties of crystalline solid-state systems.

2.4.1 Periodic Boundary Conditions

Performing DFT calculations directly on bulk crystalline solid-state systems is computationally intractable [20]. As a result, these macroscopic systems are treated as a series of repeating crystal unit cells [26] and this practice is known as applying periodic boundary conditions to the system of interest. Using this framework, properties (such as converged energies) of one unit cell are calculated and then propagated throughout the whole system [26].

2.4.2 Plane Waves and Bloch's Theorem

Imposing periodic boundary conditions enables us to use plane wave formulation combined with Bloch's theorem to determine the wavefunction of the crystal structure [26]. This makes DFT calculations more practical on a bulk system. A plane wave is a type of wave whose phase is perpendicular to its direction of propagation [20] and its equation of motion $F_{\mathbf{k}}(\mathbf{r})$ is given by

$$F_{\mathbf{k}}(\mathbf{r}) = e^{i\mathbf{k}\cdot\mathbf{r}} \quad (2.20)$$

where \mathbf{k} is the crystal momentum and \mathbf{r} is the position of the wave. Using this equation of motion, we can apply Bloch's theorem, which states that a wavefunction can be written as a product of a periodic potential and a plane wave, to determine the wavefunction of the system [20]. As discussed in Section 2.1.1, that the potential $u(\mathbf{r})$ of a crystal lattice is periodic and is given by

$$u(\mathbf{r}) = u(\mathbf{r} + \mathbf{R}) \quad (2.21)$$

where \mathbf{R} that corresponds to the periodicity of the crystal lattice. The wavefunction of the crystal lattice at a given crystal momentum is therefore

$$\psi_{\mathbf{k}}(\mathbf{r}) = e^{i\mathbf{k}\cdot\mathbf{r}} u(\mathbf{r}) \quad (2.22)$$

To simplify this wavefunction further, we can decompose our periodic potential into its component frequencies by taking its Fourier transform [20]

$$u(\mathbf{r}) = \sum_{\mathbf{G}} c_{\mathbf{G}} e^{i\mathbf{k}\cdot\mathbf{G}} \quad (2.23)$$

where $c_{\mathbf{G}}$ are coefficients, and \mathbf{G} is the reciprocal lattice vector [20]. This formulation can also be thought of as the periodic potential of the crystal being expressed using a basis set of plane waves that are discretized by the reciprocal lattice vectors of the crystal [26]. This allows to express the wavefunction of the crystal system given by 2.22 as

$$\psi_{\mathbf{k}}(\mathbf{r}) = e^{i\mathbf{k}\cdot\mathbf{r}} \sum_{\mathbf{G}} c_{\mathbf{G}} e^{i\mathbf{k}\cdot\mathbf{G}} \quad (2.24)$$

2.4.3 Pseudopotentials

The DFT approach involves constructing a potential which is a sum of the kinetic, potential, and exchange-correlation interactions; these potentials form an effective-potential that functions as an external potential acting on the system [26]. This formulation is applied to electron-only calculations where core and valence electrons are treated in the same manner [26]. However, in large bulk crystal systems, a different approach involving pseudopotentials is taken.

Pseudopotentials divide electrons of a system into valence electrons and core electrons [20]. A pseudopotential allows replacement of the highly oscillatory core-electron wave functions, due to their treatment as plane waves, with a smoother potential. A pseudopotential divides an atom into the valence and core regions. Using the fact that core electrons are usually tightly bound to their nuclei and do not contribute to chemical processes, such as binding, atoms can be treated as a large ionic cores that have interactions with valence electrons [26].

This framework is also supported by the fact that valence electrons are usually the ones involved in chemical binding processes [26]. By applying this approximation to bulk solid-state crystalline materials, we can treat these ion cores as fixed while the

valence electrons are free. This means that the core electrons do not contribute to the system's structural properties when carrying out DFT calculations [26]. A pseudopotential hence replaces oscillatory core-electron wavefunctions with a smoother potential by only considering the wavefunctions of the valence electrons beyond a cutoff radius; the ionic core is treated as an effective external potential instead [26]. These valence wavefunctions hence characterize the whole system.

2.4.4 Brillouin Zone Sampling

The last facet of DFT for periodic systems we need to account for is the sampling scheme used to calculate electronic properties. Specifically, we need to know how many position vectors to account for in the unit cell of the periodic crystal that is being modelled. To do so, we sample a set of crystal momentum \mathbf{k} vectors within the the Brillouin zone, or reciprocal space, of this cell. This set of vectors is known as a k-point grid [20]. The method used in this thesis to sample k-points is to produce an evenly spaced array of points in each of the three dimensions of the unit cell in reciprocal space [20]. For a given unit cell, we hence have a k-point grid of $i \times j \times k$ in which i corresponds to the number of k-points being sampled in the x-axis, j in the y-axis, and k in the z-axis.

2.5 Advantages and Limitations of DFT

Density Functional Theory was chosen as the first-principles framework of this thesis for several reasons. Firstly, it aims to account for every type of electronic interaction energy in a system: kinetic, electron-nuclei, and electron-electron interactions. It also accounts for interlayer Van der Waals forces. As a result, it attempts to paint a quantum mechanically accurate and complete picture of a physical system. Additionally, it is designed for periodic solid modelling, making it an appropriate choice to study a solid-state system such as twisted trilayer graphene. However, DFT cannot perform accurate calculations for larger system sizes; it does not scale well due to the large Brillouin zone meshgrid required for meaningful results. As a result, it is unable to produce results for moiré cells with more than 200 atoms which correspond to small twist angles. This is a challenge as these small twist angles are the ones we are experimentally interested in.

Chapter 3

Computational Methods

3.1 The TriCrystal Code

3.1.1 Algorithm and Usage

Our objective was to use a Density Functional Theory (DFT) framework to analyse twisted trilayer graphene. While there are several software packages available to perform DFT calculations on solid-state systems, we used Quantum Espresso [24]. Quantum Espresso is a modular and open-source software that is used for electronic-structure calculations [12]. It prioritizes being run on massive parallel architectures using Bash scripting and analyzing CIF (Crystallographic Information Files) files [12]. It can perform several operations including ground state calculations, geometrical optimization of crystalline structures, and ab initio molecular dynamics. It can calculate several properties of crystalline structures using DFT calculations including ground state energy, density of states, and band structures.

One of the most important components of using Quantum Espresso for DFT calculations is generating input files that capture the atomic coordinates of unit cells of the systems we want to perform calculations on. This is especially true when working with layered systems where rotation is involved with one of the layers. Graduate student Tilas Kabengele, who is part of the Rubenstein group at Brown University, developed a Python program called **BiCrystal** to address this task. **BiCrystal** builds incommensurate crystal structures of twisted bilayer materials by reading CIF files and generating a corresponding Quantum Espresso input file of the structure [21].

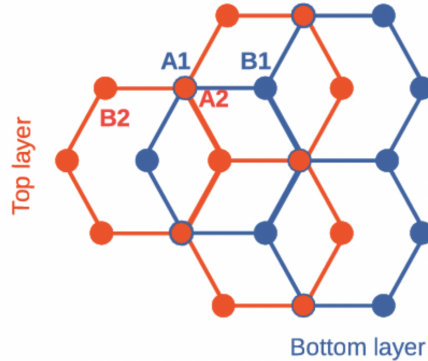


Figure 3.1: A visualization of an AB-stacked structure of bilayer graphene, the structure that is initially inputted into **TriCrystal** to generate twisted trilayer graphene structures. This figure has been adapted from [27].

For the purpose of this thesis, this original program was modified and further developed such that it could produce input files for trilayered systems instead of bilayered ones. This modified program is called **TriCrystal** and its code repository is available in Appendix A. **TriCrystal** works very similarly to **BiCrystal** with some fundamental modifications in relation to the number of atomic coordinates and layers it generates as well as how it calculates interlayer spacing using a user-specified cell vacuum parameter. **TriCrystal** is an interactive program that requires several user inputs to run. First we input a CIF file of the material we are constructing structures of. For us, this was a CIF file of AB-stacked bilayer graphene, whose structure is shown in Figure 3.1. CIF files such as these can be downloaded from databases such as The Materials Project [19].

```
***Input cif file***
cc.cif
```

Next, we input two parameters (m, n), which are used to define the Moiré supercell on our crystal structure. As established in **Bicrystal**, these parameters signify that the program needs to build a supercell that is m lattice spacings in the x-direction and n lattice spacings in the y-direction. Two chosen atoms A and B that are used to define the vertices of the supercell generated with $m=2$ and $n=1$ are shown in Figure 3.2. Once atoms A and B are chosen, the remaining vertices of the supercell, C and D, are chosen by extrapolating to generate the parallelogram unit cell of graphene. The complete Moiré supercell for graphene generated for $m=2$ and $n=1$ is also shown in Figure 3.2.

```
***Rotation parameters***
```

```
Enter m 2
```

```
Enter n 1
```

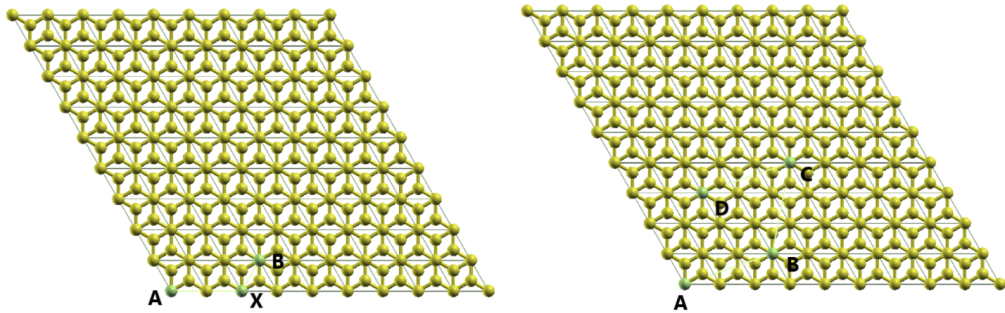


Figure 3.2: Figures of how **TriCrystal** chooses boundaries of two Moiré supercells generated for $m=2$ and $n=1$. One structure has first two vertices, A and B, highlighted (left) and the other structure has all of the vertices, A, B, C, and D, highlighted (right). These figures were adapted from [20].

The supercell is defined for the bottom and top layer in the bilayer graphene CIF file. The choice of (m,n) also helps us calculate the twist angle ϕ of the Moiré system through the following equation [20]:

$$\cos(\phi) = \frac{m^2 + 4mn + n^2}{2n^2 + 2mn + 2m^2} \quad (3.1)$$

Next, the program prompts for a user input for the vacuum cell parameter for the defined unit cell. This parameter defines an artificial periodicity along the z axis of the supercell by separating it with a vacuum. The purpose of having a larger vacuum parameter is for calculation accuracy. This parameter ensures that other atoms in the system do not affect or interfere with the unit cell and its calculations.

```
***Cell Vacuum Parameter***
```

```
Enter z 80.0
```

After several relevant parameters have been input, an initial atom on the middle and bottom layers is chosen. This initial atom corresponds to the A-th vertex in the unit supercell as shown in Figure 3.2 for each layer. The program prints out the crystal coordinates of two atoms in the bottom and middle layers and then prompts the user to choose the A-th vertex of each layer. Although we are building a twisted trilayer system, we only initially work with bilayer coordinates as the middle layer is the rotated one. The final layer is overlayed on top at the end of the program as it has the same X and Y coordinates as the bottom layer with different Z coordinates. Once the A-th atom for the bottom and middle layers has been specified, the parallelogram unit cell using the inputted (m,n) parameters is completed.

```

Initializing atoms...

Initial MIDDLE atoms..
Atom No. 1    c    [0.  0.  0.5]
Atom No. 2    c    [0.66667 0.33334 0.5      ]

Initial BOTTOM atoms..
Atom No. 3    c    [0.  0.  0.]
Atom No. 4    c    [ 3.33330000e-01  6.66670000e-01 -3.08148791e-33]

Select zeroeth MIDDLE atom
Enter Atom No. 1

Select zeroeth BOTTOM atom
Enter Atom No. 3

```

Next, a rotation to the middle layer is applied. Prior to carrying out this rotation, however, every atom's coordinates is converted from Crystal coordinates to Cartesian ones. Then, using the twist angle calculated using 3.1, a rotation matrix $R(\phi)$ is applied to modify each atom's coordinates in the middle layer [20]

$$R(\phi) = \begin{bmatrix} \cos(\phi) & -\sin(\phi) \\ \sin(\phi) & \cos(\phi) \end{bmatrix} \quad (3.2)$$

This rotation can often result in some of the twisted layer's atoms falling outside of the defined boundaries of the unit cell. To tackle this problem, the program removes these atoms entirely. The final step of **Tricrystal**'s algorithm involves overlaying a third layer on top of the twisted bilayer structure, and modifying each layer's Z coordinates such that they are compatible with the input vacuum parameter. The interlayer spacing of our system is affected by the vacuum parameter; a larger vacuum parameter corresponds to a larger interlayer spacing and vice versa. The target interlayer spacing is 3.36 Angstroms. Using the XCrySDen visualization software, several vacuum parameters were evaluated to determine an approximate empirical relationship between the vacuum parameter Z_{cell} and interlayer spacing $I_{spacing}$

$$I_{spacing} = \frac{3.36}{Z_{cell}} \cdot 2 \quad (3.3)$$

from which the Z coordinates of each layer are calculated. The middle layer was set to have a Z coordinate of 0.5 and added and subtracted the calculated $I_{spacing}$ to generate the Z coordinates of the top and bottom layers. After this calculation, the third layer was overlayed on top of the twisted middle layer by making a copy of the X and Y coordinates of the bottom layer and inputting the calculated Z coordinate value. Once the system's coordinates are finalised, its corresponding Quantum Espresso file is output.

3.1.2 Example Structure Visualisation

An example of the twisted trilayer graphene structure that the **TriCrystal** program can produce can be visualised using the XCrySDen software. XCrySDen reads Quantum Espresso input files and provides visualisations of structures. Figure 3.3 and 3.4 shows an example of a twisted trilayer graphene structure generated using **TriCrystal**.

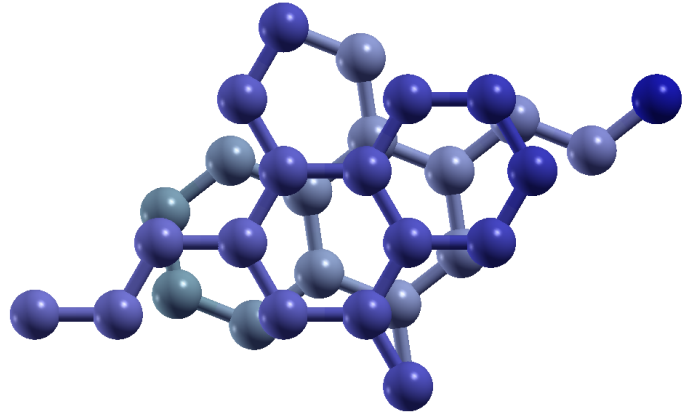


Figure 3.3: A twisted trilayer graphene structure generated using **TriCrystal** with a twist angle of 21.79° , or parameters of $m=2$ and $n=1$. This is a view of the structure from the top down and has been generated using XCrysDen.

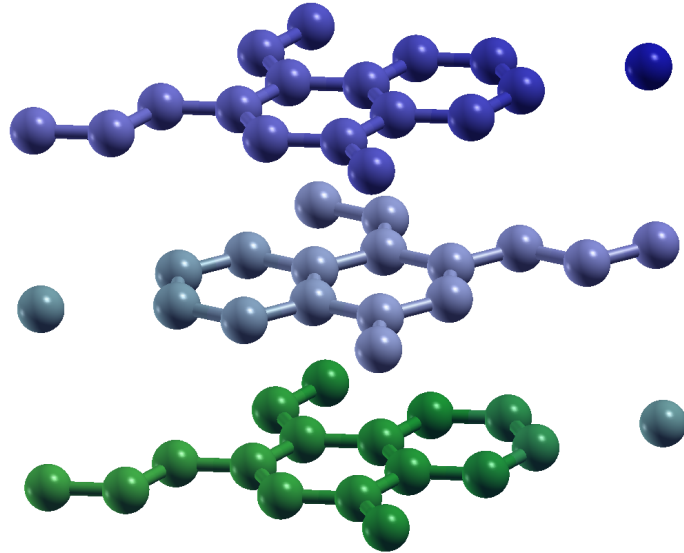


Figure 3.4: A twisted trilayer graphene structure generated using **TriCrystal** with a twist angle of 21.79° , or parameters of $m=2$ and $n=1$. This is a view of the structure shown in Figure 3.3 from the side and has been generated using XCrysDen. Each layer has been differentiated by colour; the middle layer has been twisted.

3.2 Converging Structural Parameters

For the purpose of this thesis, two different multilayer graphene systems were analysed: a 4-atom unit cell of AB-stacked bernal bilayer graphene and a 42-atom twisted trilayer graphene system with a twist angle of 21.79° . It is important to note that the twist angle of the trilayer system is far larger than the ones used experimentally. We were restricted to this angular range due to the fact that smaller twist angles correspond to a larger number of atoms in the system and calculations for systems with > 200 atoms are too computationally expensive to execute using Oscar, Brown University's cluster. These systems were chosen to perform baseline DFT calculations to ensure that expected theoretical results were seen at higher angles and in bernal systems before proposing a method to approach smaller twist angles.

The objective was to generate the band structures of these systems using Quantum Espresso. Prior to being able to carry out these calculations, however, four key structural parameters of these geometries were converged using self-consistent field **scf** calculations. The **scf** method involves using an approximated Hamiltonian to solve the Schrödinger equation to obtain a more accurate set of orbitals and solving the Schrödinger iteratively again until the energy of the system converges, a scheme described in Section 2.3.3.

The first two parameters that were converged were the energy cutoffs used to bound the wavefunctions used in our SCF calculations. These parameters are called *ecutwfc* and *ecutrho* in Quantum Espresso. *ecutwfc* corresponds to the highest possible kinetic energy of the wavefunctions, or orbitals, used to describe the system. A higher *ecutwfc* value means that a larger number of wave functions will be used to represent the orbitals to iteratively solve the Schrödinger equation, resulting in a more accurate description of the system. *ecutrho* corresponds to the kinetic energy cutoff for the charge density and pseudopotential we use in our SCF calculation. The *ecutrho* value is usually 10 times the *ecutwfc* value. To determine which (*ecutwfc*, *ecutrho*) pair to choose, several pairs of energy cutoffs were tested by running SCF calculations. The converged energy of each pair of energy cutoffs were plotted against the *ecutwfc* value. The cutoff for which the SCF energy converged was chosen as the final value for this parameter. An example of one of these plots for a 42-atom system is provided in Figure 3.5.

The next parameters that were optimised were the *nk1* and *nk2* values of the K-Point grid. The *nk3* value was set equal to 1. These three values correspond to the number of points sampled from the Brillouin zone of the chosen system in the x-axis, y-axis, and z-axis. The *nk1* value was set equal to the *nk2* value while the *nk3* value was set to 1.

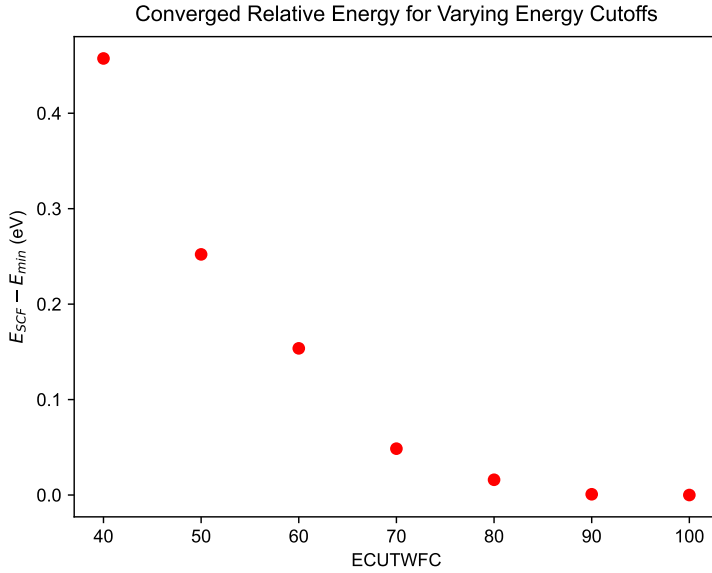


Figure 3.5: Converged energies for 7 ($ecutwfc$, $ecutrho$) pairs for a twisted trilayer graphene system with a twist angle of 21.79° , or parameters of $m=2$ and $n=1$. Convergence is reached approximately at ($ecutwfc=90$, $ecutrho=900$).

Different K-Point grid configurations were tested using SCF calculations. To determine which K-point configuration to use, the SCF energy for each configuration was plotted against the $nk1$ and $nk2$ value. The configuration for which the energy converged was chosen as the final parameter. An example of one of these plots for a 42-atom system is provided in Figure 3.6.

The last parameter converged was the Z-Cell Parameter. This is denoted as $v3(3)$ in the Quantum Espresso documentation and represents the spacing between each unit cell of TTG in the crystal lattice in Bohr. A larger Z-Cell Parameter, also known as the cell vacuum parameter, corresponds to a larger interlayer spacing. A larger vacuum parameter also corresponds to less interactions between successive unit cells of the crystal structure. Similar to the way other parameters were converged, several Quantum Espresso input files with varying cell vacuum parameters were generated. SCF calculations were run on these files and the converged energy was plotted against the vacuum parameter to determine which parameter value the energy was converging for. This plot can be visualised in Figure 3.7.

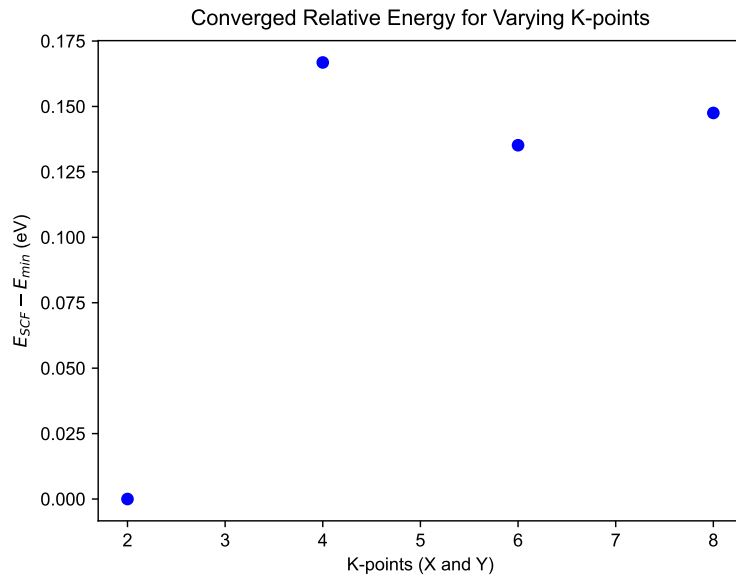


Figure 3.6: Converged energies for 4 K-Point grid values ($X, Y, 1$) for a twisted trilayer graphene system with a twist angle of 21.79° , or parameters of $m=2$ and $n=1$. Convergence is reached approximately at $(6, 6, 1)$.

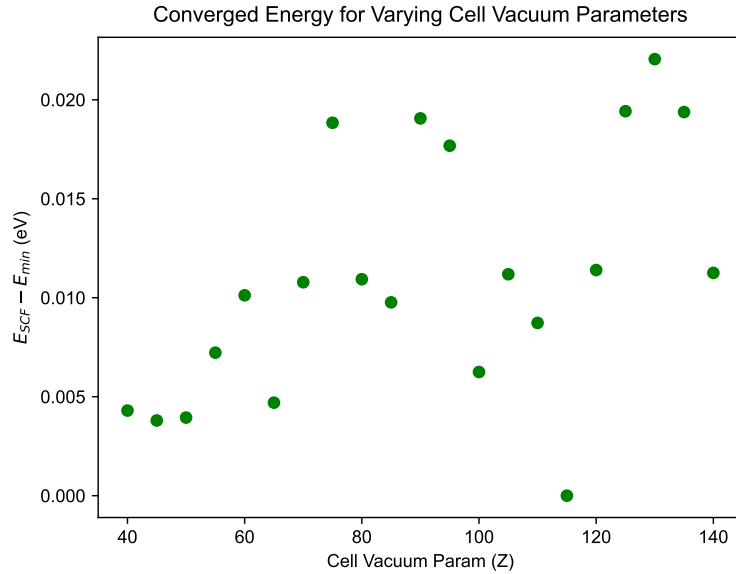


Figure 3.7: Converged energies for 21 cell vacuum parameters values for a twisted tri-layer graphene system with a twist angle of 21.79° , or parameters of $m=2$ and $n=1$. Convergence is reached approximately at $Z=80.0$.

Unlike the other parameters, there is a lot of fluctuation within the energies and clear convergence can only be seen at lower vacuum parameter values. One reason why this could be happening is due to the approximations made when calculating interlayer spacing to generate the Quantum Espresso input files. While this is an issue in the short term, in the long-term we will further optimise the interlayer spacing by relaxing the structure of our geometries. A summary of the converged parameters chosen for the two geometries of interest in this thesis are provided in Table 3.1.

<i>System</i>	Moiré Angle ($^{\circ}$)	Atoms	(<i>ecutwfc</i> , <i>ecutrho</i>)	K points	Z cell
AB-stacked bilayer	0.00	4	(80, 800)	(10, 10, 1)	25.0
Twisted trilayer	21.79	42	(90, 900)	(6, 6, 1)	80.0

Table 3.1: A summary of converged parameters for two different multilayer graphene geometries.

3.3 Generating Band Structure

Generating the band structure of a system is a multi-step process in Quantum Espresso. First, a **relax** calculation was performed, which is essentially a geometry optimization of the atomic coordinates in the z-axis of the system to optimize interlayer spacing. Next, using the optimized coordinates from this calculation, an **scf** calculation was performed. Then, the next step involved a non-SCF calculation. This calculation aims to find a solution to the Schrodinger equation by iteratively minimizing the density charge functional until a specified bound in the energy difference between two given iterations is reached. **nscf** calculations require a much denser K-point sampling grid along the X and Y axes. A K-Point grid with X and Y values that were 5 times larger than their converged values were used here. Lastly, a **pw.x** calculation was performed. This step determined the finalised Kohn-Sham eigenfunction and eigenvalues of the system [8]. During this step, a number of bands *nbnd* was specified. After this, a **bands** post-processing step was run, from which the band structure of our system was obtained.

Chapter 4

Experimental Methods

4.1 Flake Exfoliation

4.1.1 The “Scotch-Tape” Method

The objective of this experimental method was to isolate a single layer or a small number of layers of a bulk material. This was done by placing a piece of bulk material of diameter 1-2 mm on top of a 10cm piece of Scotch Magic Tape. This tape was then folded and peeled backwards methodically, creating a square of exfoliated bulk material of approximate size 1cm x 1cm. Depending on the bulk material exfoliated, Scotch Greener Tape was also incorporated in this process. This process is known as the *Scotch-Tape Method*.

4.1.2 Silicon Wafer Cleaning

Exfoliated bulk crystals are stored on top of Silicon wafer chips of approximate size 1cm x 1cm. To do so, large Silicon wafers were diced into smaller square chips of desired size using a diamond-head cutter and tweezers. The diamond-head cutter was used to make incisions and the tweezers were used to press down on either side of each incision and split the larger wafer. Periodically, a Nitrogen pump was used to blow air on the chips to clean off impurities from their surfaces such as smaller shards of snapped Silicon wafer. Another step we took to prepare a given Silicon chip was to apply a plasma treatment to it using a Plasma Etcher. This was done to remove any other residue material on the surface of the chip using a plasma created from Oxygen. Each chip was placed on a glass slide and put through a 10 second etching cycle prior to flake exfoliation.

4.1.3 Graphite

Using the *Scotch Tape Method*, a 1cm x 1cm square of exfoliated bulk Graphite crystal was obtained on a piece of Scotch Magic Tape. This tape was then placed on top of a Silicon chip that had undergone plasma treatment. A long Q-tip was used to slowly press the square of exfoliated graphite on the tape onto the Silicon chip. This chip was baked on a magnetic hotplate stirrer for 2 minutes at 100°C. Once the chip had cooled after baking, tweezers were used to rapidly remove the piece of tape covering the Silicon chip, leaving behind a square of exfoliated Graphite flakes on its surface.

4.1.4 Boron Nitride

A slightly modified version of the *Scotch Tape Method* was used to exfoliate bulk Boron Nitride (BN). A 10cm piece of Scotch Greener Tape was prepared and a small flake of BN crystal was placed on top. BN crystals do not stick as easily to Magic Tape which is why Greener Tape was used instead. As described by the *Scotch Tape Method*, this tape can be folded and peeled backwards, leaving behind a 1cm x 1cm square of exfoliated crystal on the tape. This is known as the mother tape. We cut a smaller piece of Scotch Greener Tape and exfoliate BN flakes from the mother tape as shown in Figure 4.1. These smaller tapes are known as daughter tapes. Each mother tape produced 2 daughter tapes. Each tape containing exfoliated BN crystals should be placed on top of a diced Silicon chip. A long Q-tip was used to slowly press the square of exfoliated BN on the tape onto the Silicon chip. Then, this tape was peeled from the Silicon chip very slowly at a 90° angle to the horizontal using a pair of tweezers to hold the chip down. In contrast to the graphene exfoliation which involved a rapid ripping back of the tape, this peeling process took 5 minutes to complete, leaving behind a square of exfoliated BN crystals on the chip's surface.

4.1.5 Cataloguing and Optical Microscopy

An optical microscope was used to scan over Silicon chips containing exfoliated BN and graphite crystals. Potentially useful flakes for building devices were identified and catalogued using various settings such as LUTs (Lookup Tables that are used to pseudo-colour images by creating different colour channels) and measurement tools available on the microscope's software. For example, monolayer graphene pieces $> 40 \mu\text{m}$ were identified for the twisted trilayer graphene portion of our device. Similarly, BN flakes

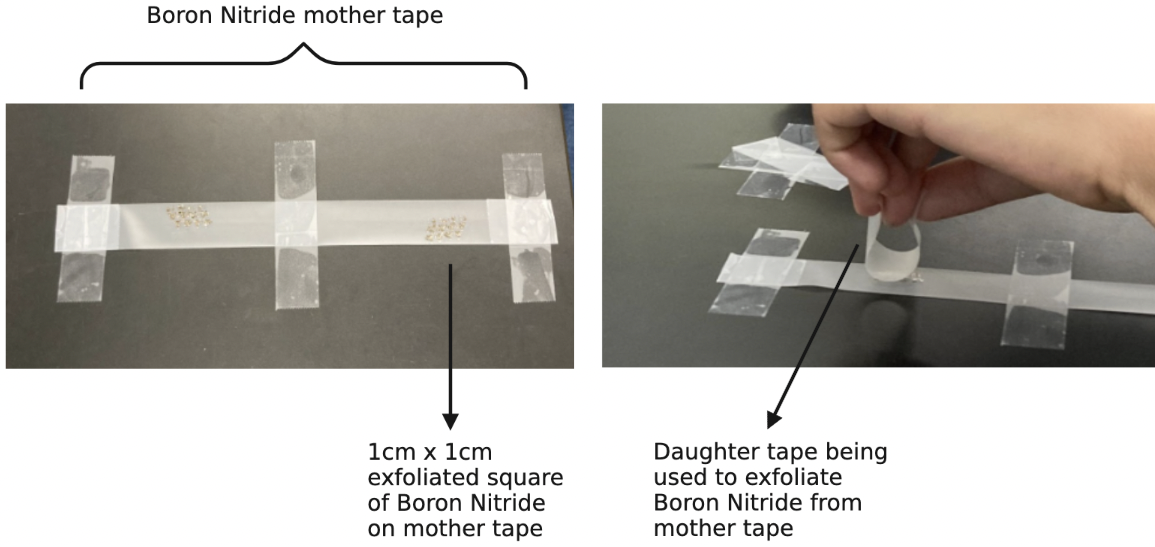


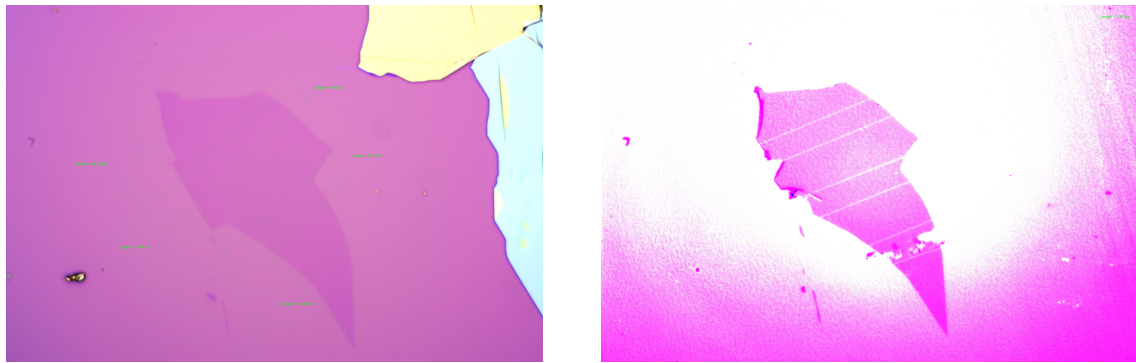
Figure 4.1: Exfoliation of Boron Nitride flakes using a prepared mother tape (left) and the use of daughter tapes to exfoliate flakes from the mother tape (right).

required for top gates and bottom gates were also identified. These flakes were catalogued on a shared drive and were used to plan the complete device.

4.2 Atomic Force Microscopy

4.2.1 Thickness Estimation

We employed the Atomic Force Microscope (AFM) for two distinct processes: flake scanning and lithography. The first process was used to qualify homogeneity and estimate thickness of relevant exfoliated flakes. The 'Tapping' or non-contact mode on the AFM was used to scan flakes. In non-contact mode, the AFM tip oscillates on top of the surface while scanning. The force interactions between the tip and surface while causes this oscillation amplitude to vary. Using a feedback loop, surface topology can be reconstructed using these changes in amplitude. The scanned flakes were analyzed using the Height Sensor data collected by the AFM. The change in height between the edge of each flake and the Silicon chip's surface was measured for each flake used to construct the device.



(a) Image of exfoliated monolayer graphene. (b) LUT image of cut monolayer graphene.

Figure 4.2: A comparison of a flake of exfoliated monolayer graphene before (a) and after (b) lithography has been carried out on the flake using an AFM. Both images were taken at $\times 100$ magnification using an optical microscope.

4.2.2 Cutting and Lithography

The second way in which the AFM was used was for lithography and nano-patterning on graphene. Specifically, it was used to cut monolayer graphene into three different layers. To do so, the AFM tip was first manually changed from a scanning tip to a cutting tip. Then the 'Nanoman' package on the AFM was used to perform cutting using this tip in contact mode. In contact mode, the tip touches the surface while imaging. Sacrificial regions and layers for a twisted trilayer graphene device were outlined and cut using this feature. An example of what these cut regions look like on a piece of monolayer graphene is provided in Figure 4.2.

4.3 Device Stacking

4.3.1 PPC and PC Preparation

Prior to heterostructure device assembly, each flake required for the TTG device was prepared accordingly. Monolayer graphene was cut using the AFM. The remaining flakes, e.g. the top BN and bottom BN were identified using flake catalogues and their relative stacking positions were planned on a transparent plastic sheet. A summary of all layers required for the device are showcased in Figure 4.3. The pieces of exfoliated crystal surrounding each target flake were cleaned using a trash pickup mechanism involving polypropylene carbonate (PPC). Then, each flake was picked up using a polycarbonate (PC) polymer. These polymers were prepared on a specific transfer slide structure. The

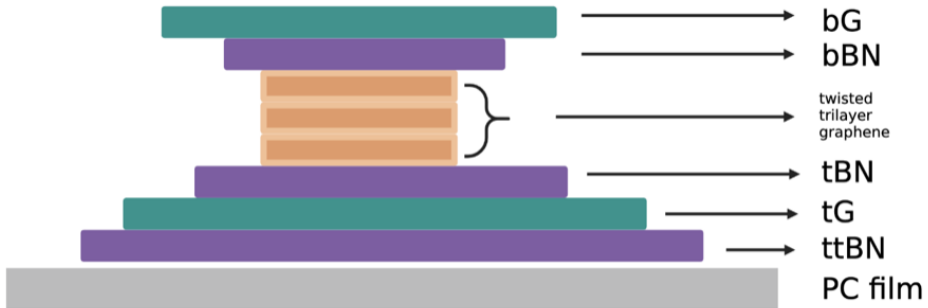


Figure 4.3: A summary of all of the layers required to construct a twisted trilayer graphene device. Here, *t* corresponds to top and *b* corresponds to bottom. *BN* signifies Boron Nitride and *G* signifies Graphite.

transfer slide consisted of a small square of polydimethylsiloxane (PDMS) glued on a glass slide. A piece of transparent Scotch tape was stretched around the PDMS block and taped onto the slide.

First let us discuss how PPC was prepared for trash pickup. A clean Silicon chip was placed on the lab's centrifuge and a vacuum was turned on to hold the chip in place. Then, 1-2 drops of PPC were deposited into the center of the chip via a pipette. The chip was then spin-coated using the centrifuge. Once the PPC was evenly covering the chip, it was baked at 90°C for 1 minute. To transfer this PPC from the chip to the slide, a small portion of the corner of the PPC was scraped off from the chip using a mini razor blade.

Then a hole was punched into a piece of tape using a hole-puncher. This tape was placed on top of the PPC coated chip and slowly pulled away diagonally from the scratched off corner. This PPC containing tape is placed on top of the PDMS block on the transfer slide. This slide is then baked again at 90°C for 1-2 minutes to reduce wrinkling on the PPC film. This PPC acts as a sticky film that can pick up exfoliated flakes using the transfer station. The PPC transfer slide was largely used for trash pickup surrounding a target flake.

The second type of polymer that was used to pick up flakes, specifically for device assembly as opposed to trash pickup, was PC. To prepare PC, first a transfer slide was obtained as described above. However, unlike the transfer slide for the PPC, no Scotch tape was placed around the PDMS. The PDMS stamp was checked under an optical microscope for fibres and dust particles. These were removed using a nitrogen pump

or the sticky side of a piece of tape. Since the PC film will be placed right on top of the PDMS, it was critical to ensure that little to no particle matter was on the PDMS stamp to avoid deformities on the PC film and ensure its uniformity.

Next, two clean glass slides were obtained and 13-20 drops of PC solution was deposited onto one end of one of the slides using a pipette. The edge of the glass slide without any PC was then vertically lowered towards the slide with the PC and gently placed on top. Once contact between the slides was made and the PC was sandwiched between the two equal portions of the slides, they were pulled apart in opposite directions. This is known as the *Sandwich Technique*. These slides were then left to dry. Once dry, a homogenous hole-punch sized area was identified on the dried film on these slides. Using a razor blade, a square was cut surrounding this identified area and the remaining PC was scraped off the slide.

We then punched a hole into a 5cm piece of Scotch Magic tape and this tape was placed on top of the smooth square of PC. This tape was pulled off from the slide from both sides to ensure that no wrinkles formed on the PC and placed on top of the PDMS. The transfer slide was then baked at 180°C on the magnetic hotplate stirrer for 2 minutes. At this point, the film was once again examined under the optical microscope to ensure that it had the ideal consistency and homogeneity. An ideal PC film contains no wrinkles, tearing, or dirt and the bubbles present on the edges should not be converging to the center. This is important to confirm as the film shape can morph over time and it should be making as much contact with the PDMS as possible.

4.3.2 Device Assembly Through Transfer Station

We used the prepared PC and PPC for device assembly using the transfer station. There are two steps involved in device assembly: trash pickup and flake pickup. Trash pickup is carried out to ensure that the area surrounding a target flake is as clean as possible so that less unnecessary flakes are picked up during stacking. We used PPC for this process. The transfer slide with the PPC was first inserted into its respective slot on the transfer station facing downwards and fixed into place. The temperature of the transfer station was set to 41°C. The Si chip with our desired target flake was fixed into its position on the station under the transfer slide and a vacuum was turned on to hold it in place.

The transfer station has a mechanical control to manipulate the positioning of transfer slides. This mechanical control was used to slowly lower the transfer slide until it touched the surface of the Si chip. The chip-slide initial contact point is known as the touchdown point and can be identified using the camera attached to the transfer station microscope. On this camera we observe Newton rings, or concentric circles of varying colours formed from light interference at different angles, forming at the touchdown point. The touchdown point was positioned right above a target flake.

If the touchdown point completely covered the trash required to be picked up, a fast retraction technique was used to lift the transfer slide from the Silicon chip surface. Alternatively, if the trash was outside the boundary of the touchdown point, its circumference was expanded either by raising the temperature of the PPC via the transfer station (with a maximum allowed temperature of 45°C) or by lowering the slide further to push more strongly against the Si surface. Then, a fast retraction technique was used again to lift the PPC from the chip surface.

In addition to trash pickup, the transfer station was used for heterostructure device assembly through flake pickup and stacking. PC was used for the device stacking process. The PC transfer slide was controlled via the transfer station in the same manner the PPC transfer slide was handled. Once more, we carried out a PC touchdown on the surface of a Si chip; the touchdown point was ensured to be as uniformly circular as possible. This was done to guarantee that the Newton rings formed by the touchdown point would run parallel to the AFM cuts made on our specific flakes to avoid tearing and folding flakes.

To pick up flakes, we expanded the PC touchdown point solely through temperature control. Specifically in increments of 0.1°C - 0.5°C. The goal is to ensure that the Newton rings expand at a constant rate. For all flakes except for the initial Boron Nitride one, we operated in a temperature range of 45°C - 180°C. For the ttBN (top-top Boron Nitride), however, we started at a temperature of 70°C. This is because the Van der Waals forces between two layers in close contact allow flake pickup to happen at lower temperatures. However, since these forces do not exist for the first layer, the Boron Nitride needs to stick to the PC in order to be lifted.

Once a flake was picked up, which happens when the entire touchdown point covers a flake, a temperature-controlled technique is used to pick-up the stack. The temperature of the transfer station is reduced to a minimum of 40°C, once again in increments of 0.1°C - 0.5°C to ensure that the Newton rings recede at a constant rate, until the touchdown point is small and does not cover the target flake anymore. Then, a fast

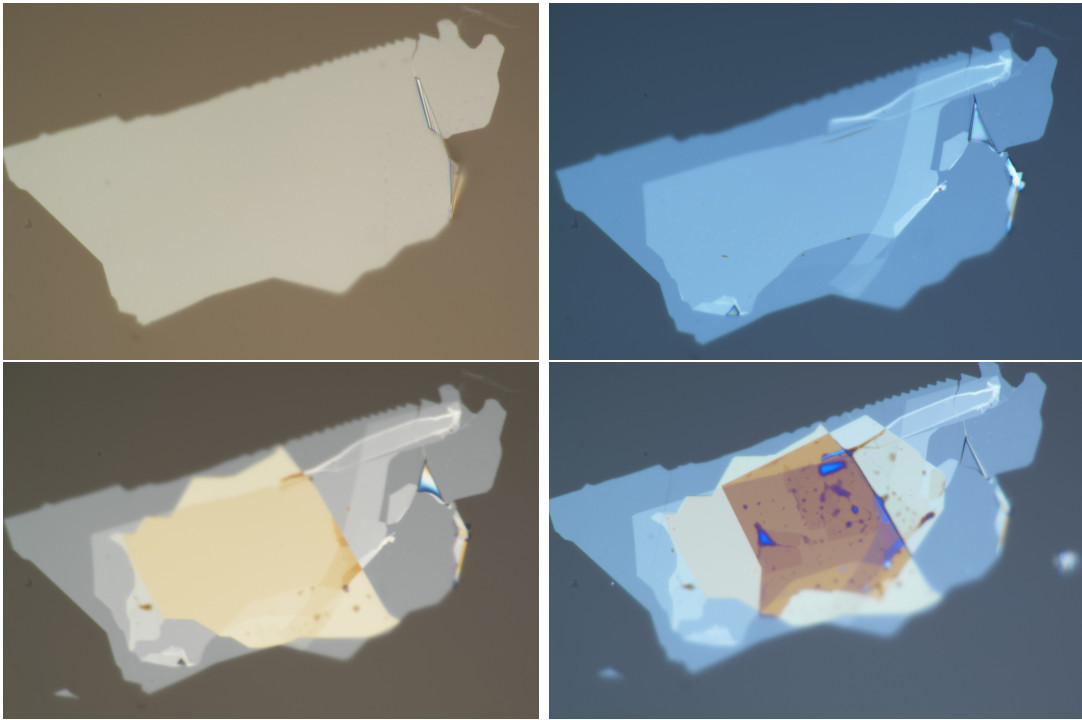


Figure 4.4: Optical images of the stacking progression of our device on the PC film / glass slide taken at a $\times 100$ magnification using the optical microscope. Initially, the top-top Boron Nitride (top-left) was picked up. Then, the top-Graphite gate was added (top-right). Next, the top-Boron Nitride was picked up (bottom-left). Then, the twisted monolayer graphene layers were stacked alongside the bottom-Boron Nitride (bottom-right).

retraction technique was used to lift the transfer slide from the Si chip. The intended stack is planned on a transparent sheet of plastic and is used to align each successive flake being picked up. Between each flake pickup, an optical microscope is used to image the stack and document the stacking progression. A portion of the stacking progression of our device is shown in Figure 4.4. While a lot of the layers can be seen optically, we can visualise the much thinner twisted trilayer graphene layers using an LUT filter, as shown in Figure 4.5.

Once all the flakes have been picked up by the PC, the stack is released onto a design chip (a chip designed to allow electrical contact to be made with the device). This is done by entirely melting the PC by raising the transfer station to 180°C onto the design chip. Then a fast retraction is used such that the device remains on the design chip. Lastly, the PC residue on the design chip is washed off using Acetone applied to the chip at a 60° angle for 60-90 seconds. Our released device is shown in Figure 4.6.

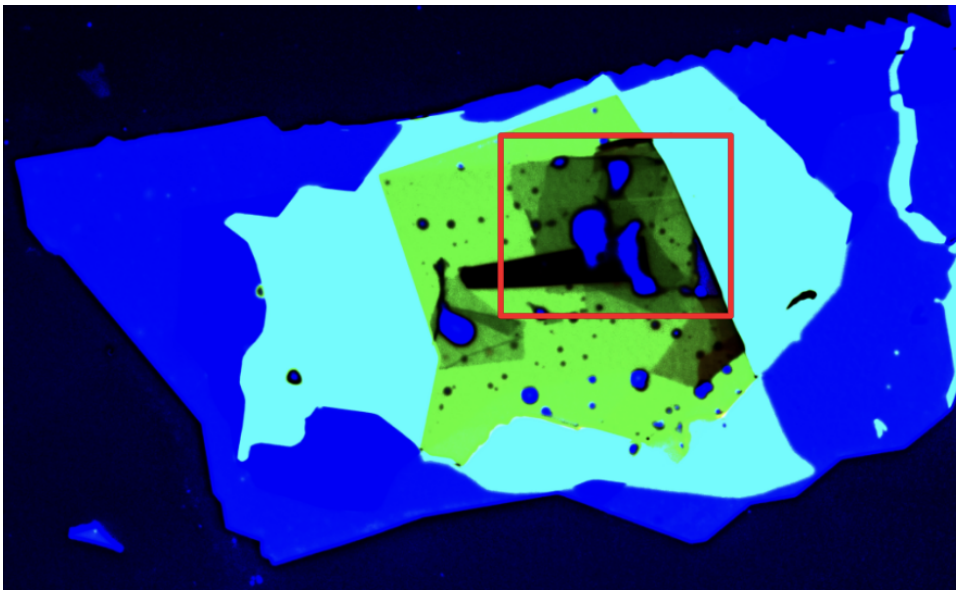


Figure 4.5: LUT image of the twisted-trilayer graphene device taken using an optical microscope at a $\times 100$ magnification. The stacked monolayer graphene layers are indicated through the red box.

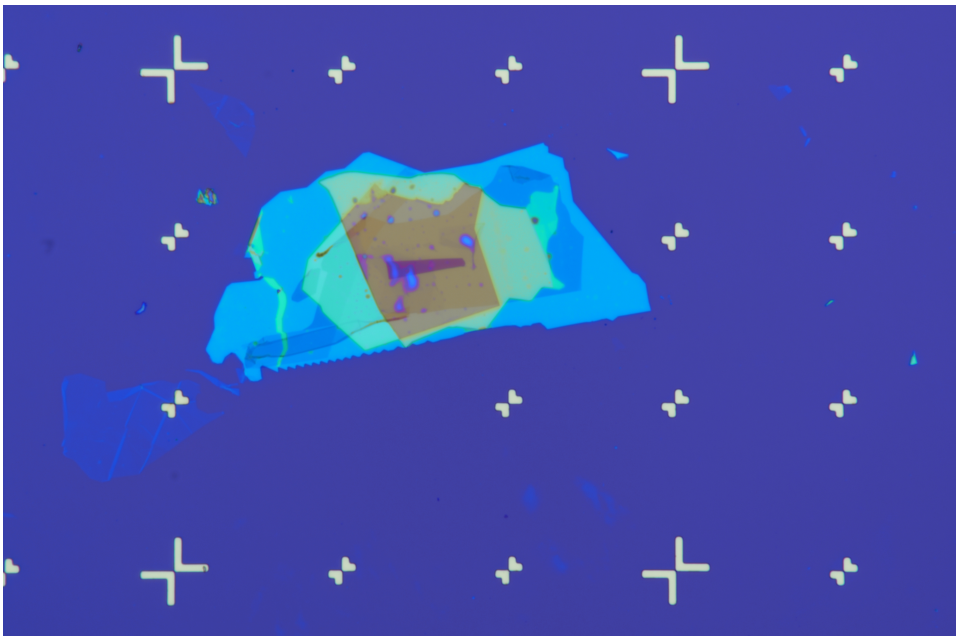


Figure 4.6: Image of released device taken using an optical microscope at $\times 100$ magnification. The visual orientation of the device is flipped vertically due to release. The alignment markers of the design chip are shown in gold surrounding the device.

4.4 Circuit Design

Once the device was stacked, DesignCAD Express 16 was used to design the microelectronic circuit for the device. Pictures of the device on the design chip in relation to the alignment markers on the chip were taken at x100 and x10 magnifications. These pictures were uploaded into the DesignCAD interface and the alignment markers on the pictures were aligned to their digitally drawn counterparts on a circuit design stencil template. First, a sunflower-shaped Hall bar with 12-13 contacts was designed on the overlapping region of the twisted trilayer graphene. Each contact into this region was extended outwards into the region of the stack only containing the top-most Boron Nitride layer. This layer is known as *the first etch* and is shown in red in Figure 4.7. *The first etch* etches away the top-most Boron Nitride and Graphite layers.

Next, another layer was constructed over top *the first etch*. This layer traced over the contacts constructed in the previous layer, but do not trace over the contact points in the sunflower-shaped Hall bar. This layer is known as *the second etch* and is shown in blue in Figure 4.7. *The second etch* etches away at all of the layers in the stack except for the bottom graphite gate. Lastly, leads were designed to connect the extended contacts from the sunflower-shaped Hall bar to electrical contacts on the design chip. Additionally, small rectangular windows were constructed on the device to connect the bottom graphite gate and top graphite gate to the electrical contacts. The layer containing the leads is known as *the third etch* and is shown in orange in Figure 4.7. *The third etch* is done to allow for gold-deposition onto the circuit to create the electrical leads for our circuit. Each lead within the circuit was designed to avoid shorting. The complete design for our device is showcased in Figure 4.8.

4.5 Electron Beam Lithography and Fabrication

The objective of Electron Beam Lithography (EBL) is to use a beam of electrons to draw customised shapes onto an electron-sensitive film. We carried out EBL to etch the design created in the previous section into our device. To do so, each layer was first isolated and transferred into individual DesignCAD Express documents to act as a guide for the EBL machine. Each layer would undergo its own *round* of EBL and etching. Prior to each etch, the device was spin-coated in polymethyl methacrylate (PMMA) and then baked at 100° for 15 minutes two times. The PMMA is an electron-sensitive film that acts as a mask onto which a stencil design can be drawn on via EBL.

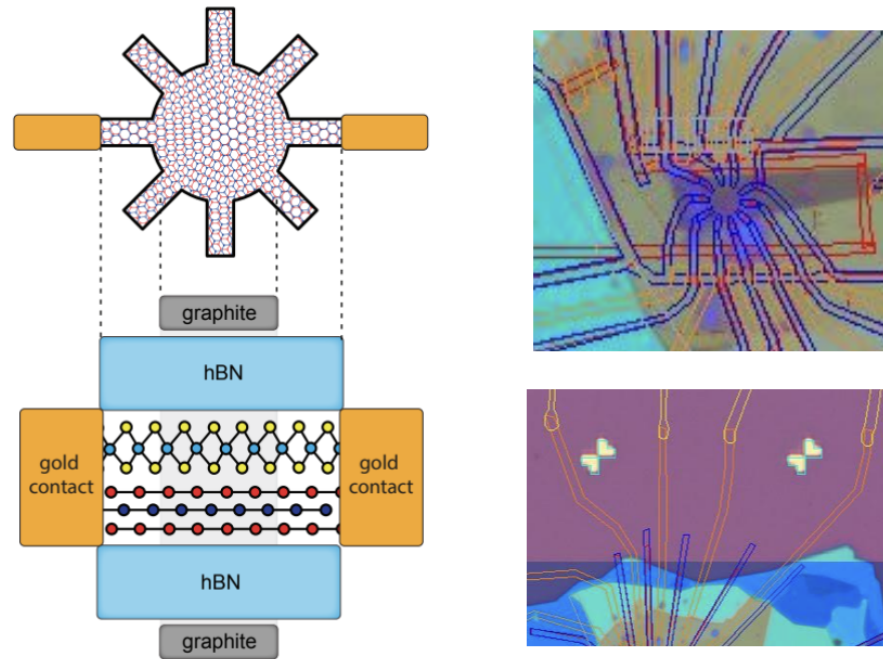


Figure 4.7: A schematic of the nanocircuit of twisted trilayer graphene containing the isolated region of interest and the gold leads (left) and the corresponding design elements on our device (right) [36].

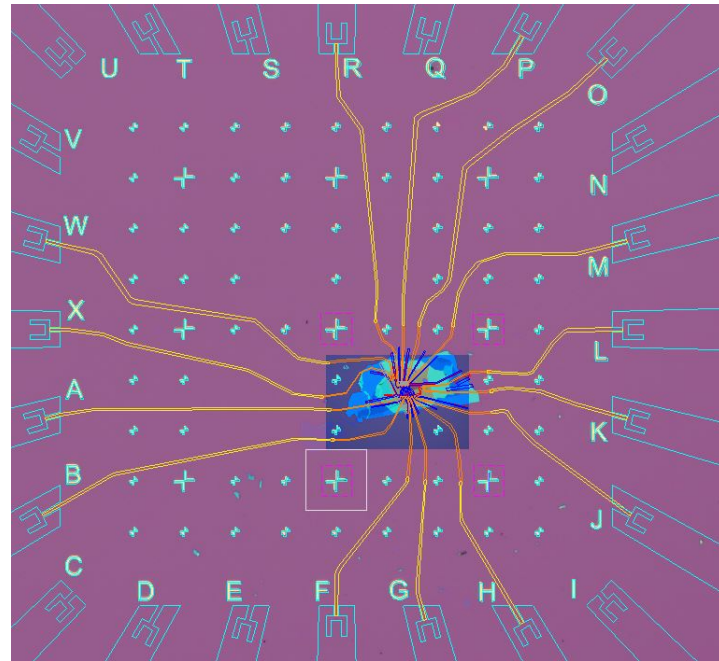
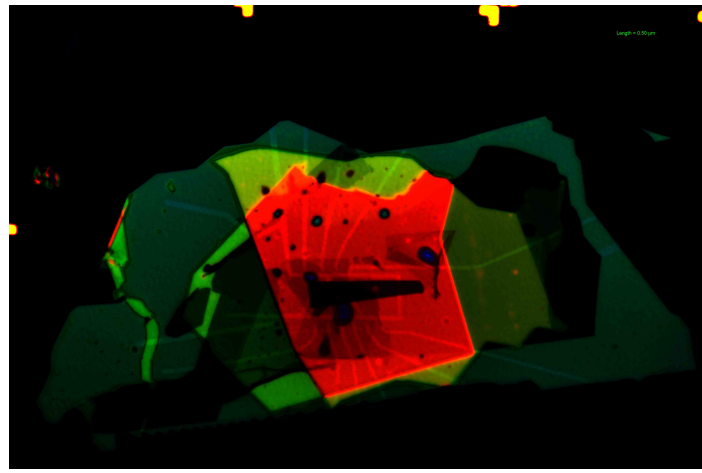


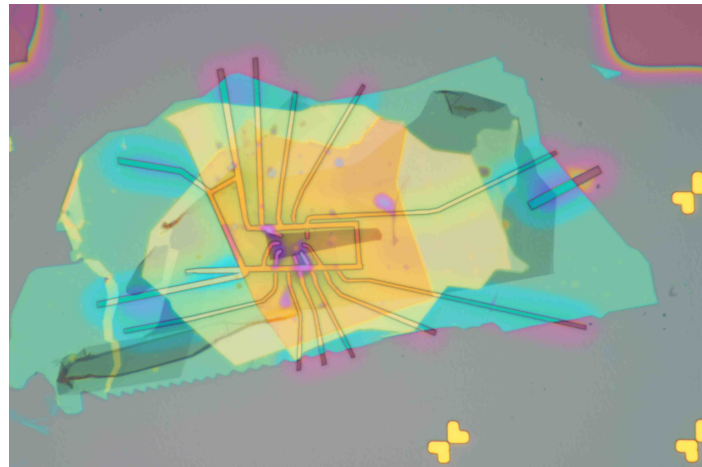
Figure 4.8: A complete schematic of our circuit design.

Each layer was converted into a run-file in the format necessary for the EBL machine and was then used to draw a given layer onto the PMMA coating our device. Then, the device underwent a process known as *development* where it was washed in a continuous stream of IPA (Isopropyl alcohol) followed by Acetone for 90 seconds each. Lastly, pictures of the device before and after *development* were taken for each round of EBL. Examples of this are shown in Figure 4.9. Once development was complete, the graduate students in Dr. Li's lab took the device to the Microelectronics Cleanroom Facility at Brown University and carried out the etching process. The first two rounds of EBL for our device were completed and the device's current state is shown in Figure 4.10.

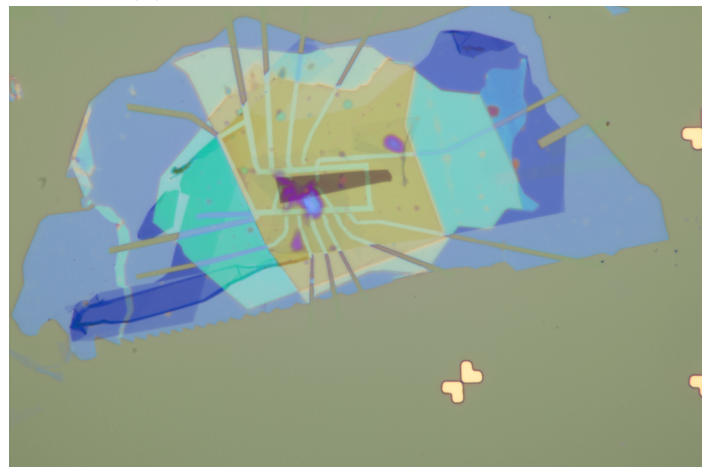
This process was then repeated for all of the etch layers present in the device except for *the third etch*. Here, rather than etching away at the layer of the device, gold deposition was carried out to create the leads necessary to make electrical contact with out device. Once the fabrication process is complete, the device is ready for transport measurements in cryogenic temperatures.



(a) LUT image of EBL of *the first etch*.



(b) Development after *the first etch*.



(c) Etching after development of *the first etch*.

Figure 4.9: Steps taken to complete the first round of EBL. These steps involve electron beam lithography of a design on the device (a), development of this design (b), and etching the design into the device (c).



Figure 4.10: Image of the device after two rounds of EBL and etching carried out in the cleanroom taken using an optical microscope with a $\times 100$ magnification.

Chapter 5

Discussion

5.1 Preliminary Results

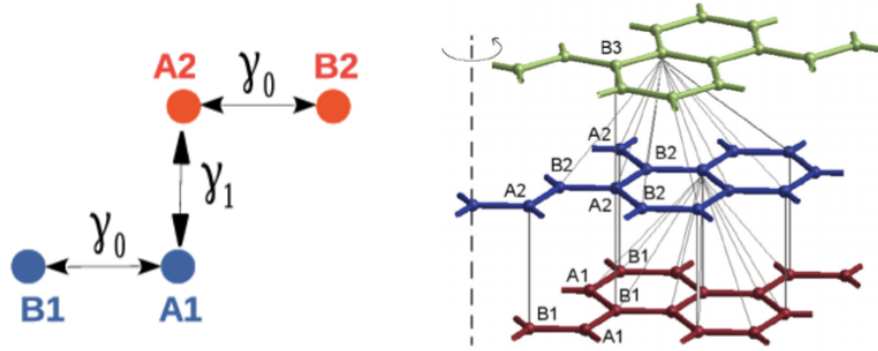


Figure 5.1: Unit cell of AB-stacked bernal bilayer graphene (left) and unit cell of ABA-stacked twisted trilayer graphene (right) [28] [30].

We have taken significant computational and experimental steps to carry out a multifaceted investigation of twisted trilayer graphene. Experimentally, we exfoliated, stacked, designed, and carried out 2 rounds of EBL and etching on a twisted trilayer graphene device that we intend to use to take transport measurements. Computationally, we designed a Python program called **TriCrystal** which can generate twisted trilayer graphene structures suitable for DFT calculations. We then converged parameters for two distinct Moiré systems: AB-stacked bernal bilayer graphene and twisted trilayer graphene with a twist angle of 21.79° . These systems were chosen to generate preliminary results to ensure we were obtaining physically consistent data before moving

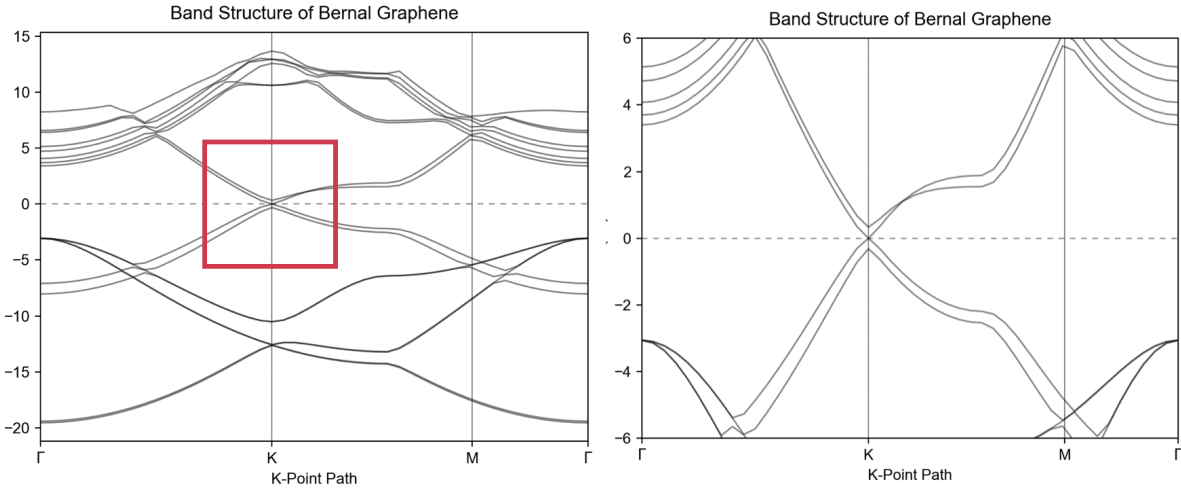


Figure 5.2: Band structure of a 4-atom unit cell of AB-stacked bernal bilayer graphene generated using Quantum Espresso. The complete band structure is shown on the left while a magnified portion in the region of interest is shown on the right.

towards smaller angle systems. The reason why we are using such a high twist angle is because its unit cell, consisting of 42 atoms, is an appropriate size to run effective DFT calculations. This section of the thesis is dedicated to performing a qualitative analysis of the calculated band structures of these systems to ensure that these initial results match theoretical expectation.

The first system we generated results for was a 4-atom AB-stacked bernal bilayer graphene system, visualised in Figure 5.1. The band structure for this system is shown in Figure 5.2. We can directly map features of this band structure to the interactions between the four atoms in the unit cell, A_1 , A_2 , B_1 , and B_2 . First we see the existence of Dirac Cone features at the K point in the Brillouin zone. We observe a two-fold degeneracy in these bands, corresponding to the fact that two monolayers of graphene are stacked on top of another. More specifically, we observe that once set of ones touch at the Fermi energy, characterising the interaction between B_1 and B_2 , while another set of cones have an energy gap between them. This dimer in the band structure emerges due to strong A_1A_2 hybridisation. Through this qualitative analysis, we confirm that this DFT-generated band structure is physically-consistent with the electronic interactions in the system.

The second system we generated results for was a 42-atom twisted trilayer graphene system with a twist angle of 21.79° . Examining this system's band structure, shown in Figure 5.3, we first observe that the structure does not have a continuous form. This

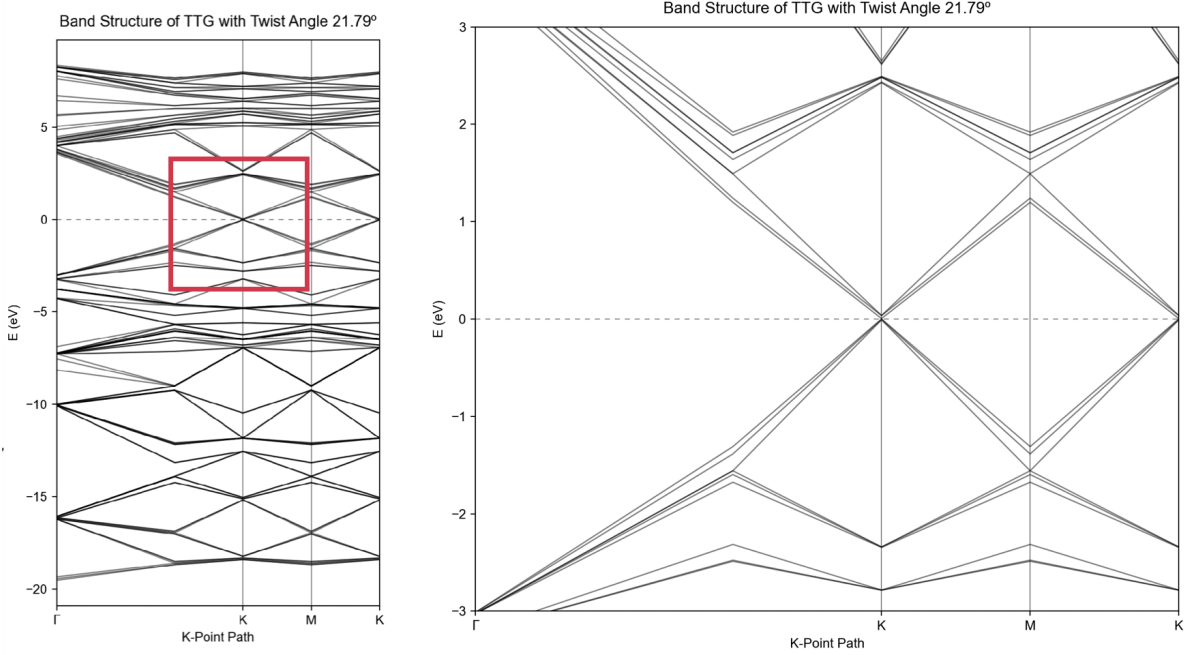


Figure 5.3: Band structure of a 42-atom system of twisted trilayer graphene with a twist angle of 21.79° generated using Quantum Espresso. The complete band structure is shown on the left while a magnified portion in the region of interest is shown on the right.

is due to the mesh-grid sampling technique applied to the system, resulting in just 6 discrete points being sampled in the X and Y dimensions of the Brillouin zone to prevent calculations from becoming computationally intractable. We once again attempt to reconcile the features of this band structure with the physical system. First, we observe three sets of Dirac Cones touching at the Fermi energy at the K point in the Brillouin zone. This degeneracy can be attributed to the three monolayer graphene layers being stacked on top of one another. Unlike the bernal structure all three Dirac cones touch at the fermi energy and this is due to the ABA stacked structure of the system generated by **Tricrystal**. There are no strong interlayer interactions or hybridisation present due to this structure as there is no direct overlap of carbon atoms on all three layers. At smaller angles, we would expect to observe the coexistence of these Dirac cones with flat band features. Specifically, we would hope to observe two sets of the Dirac cones flattening out and the other set staying the same. Additionally, if we use DFT to apply an external electric field to the system, we would see the Dirac cones being lifted from the charge neutrality point. We hence see that DFT generates results for a twisted trilayer graphene system that are consistent with its structure and electronic interactions.

5.2 Further Work

DFT becomes an especially important tool when examining small angle systems because it can attempt to explain the effects of correlation, exchange, and dispersion on the electronic properties of the system. It accounts for every interaction in the system. However, as discussed previously, directly accessing small angle systems is too computationally expensive, as these systems correspond to large Moiré unit cell sizes. To access smaller angles, we propose a cluster-based cell averaging technique. As shown in Figure 2.6, any twisted multilayer system is a combination of several different stacking arrangements. Hence when carrying out calculations for small-angle systems, we can potentially split a large Moiré unit cell into its component stacking arrangements and carry out calculations on these clusters individually. Ultimately, we can average results across all of these clusters to produce band structures for larger systems with ease. This technique is also advantageous as it allows us to use dense mesh-grids to sample the individual clusters, enabling us to produce higher resolution results too. Once we can access smaller twist angles, another avenue for further work is to calculate and plot factors such as electrical conductivity and energy band-gap as a function of twist angle to investigate where important phase changes in this system occur.

In addition to this computational research, we hope to complete the experimental facets of this project too. Specifically, we hope to complete a 3rd round of Electron Beam Lithography and carry out gold deposition on our current device to insert goals leads necessary to make electrical contact with the device. Once this fabrication is complete, we can take transport and phase measurements of our device at cryogenic temperatures. Completing these steps could result in the development of a pipeline that directly compares the experimental geometry and results generated in a lab to computational predictions, enabling to understand this novel behaviour with unprecedented accuracy.

5.3 Summary of Thesis Achievements

In this thesis, we took substantial steps to carry out a computational and experimental investigation of twisted trilayer graphene. The thesis achievements are as follows:

- Developed a user-interactive Python program called **TriCrystal** that generates twisted trilayer graphene structures to feed into Quantum Espresso and carry out DFT calculations.
- Exfoliated, stacked, designed, and carried out two rounds of EBL and etching on a twisted trilayer graphene device in the lab.
- Converged parameters for and generated band structures for a 4-atom AB-stacked bernal bilayer graphene system and a 42-atom twisted trilayer graphene system with a twist angle of 21.79°
- Proposed a cluster-based cell averaging technique to perform DFT calculations on small twist angles that correspond to usually computationally intractable system sizes.

Bibliography

- [1] *Band gap - Energy Education* — energyeducation.ca/encyclopedia/Band_gap. [Accessed 11-Apr-2023].
- [2] G.F. Bassani, G.L. Liedl, and P. Wyder. *Encyclopedia of Condensed Matter Physics*. Encyclopedia of Condensed Matter Physics v. 1. Academic, 2005. ISBN: 9780122276101. URL: <https://books.google.com/books?id=gRl8MwEACAAJ>.
- [3] University of Calgary. *Conduction band - Energy Education* — energyeducation.ca/encyclopedia/Conduction_band. [Accessed 11-Apr-2023].
- [4] Dumitru Călugăru et al. “General construction and topological classification of crystalline flat bands”. In: *Nature Physics* 18.2 (Dec. 2021), pp. 185–189. DOI: [10.1038/s41567-021-01445-3](https://doi.org/10.1038/s41567-021-01445-3). URL: <https://doi.org/10.1038/s41567-021-01445-3>.
- [5] Yuan Cao et al. “Correlated insulator behaviour at half-filling in magic-angle graphene superlattices”. In: *Nature* 556.7699 (Mar. 2018), pp. 80–84. DOI: [10.1038/nature26154](https://doi.org/10.1038/nature26154). URL: <https://doi.org/10.1038/nature26154>.
- [6] Yuan Cao et al. “Unconventional superconductivity in magic-angle graphene superlattices”. In: *Nature* 556.7699 (Mar. 2018), pp. 43–50. DOI: [10.1038/nature26160](https://doi.org/10.1038/nature26160). URL: <https://doi.org/10.1038/nature26160>.
- [7] Stephen Carr, Shiang Fang, and Efthimios Kaxiras. “Electronic-structure methods for twisted moiré layers”. In: *Nature Reviews Materials* 5.10 (July 2020), pp. 748–763. DOI: [10.1038/s41578-020-0214-0](https://doi.org/10.1038/s41578-020-0214-0). URL: <https://doi.org/10.1038/s41578-020-0214-0>.
- [8] Pranab Das. *Bandstructure Calculation • Quantum Espresso Tutorial* — pranabdias.github.io. <https://pranabdias.github.io/espresso/hands-on/bands>. [Accessed 08-Apr-2023]. 2023.

- [9] Q-Chem Developers. *5.7.3 Exchange-Dipole Model (XDM); 5.7 DFT Methods for van der Waals Interactions; Chapter 5 Density Functional Theory; Q-Chem 5.2.* <https://manual.q-chem.com/5.2/Ch5.S7.SS3.html>. [Accessed 07-Apr-2023]. 2019.
- [10] Emily V Eames. *London Dispersion Forces* — chem.libretexts.org. [https://chem.libretexts.org/Bookshelves/General_Chemistry/General_Chemistry_Supplement_\(Eames\)/Phases_and_Intermolecular_Forces/London_Dispersion_Forces](https://chem.libretexts.org/Bookshelves/General_Chemistry/General_Chemistry_Supplement_(Eames)/Phases_and_Intermolecular_Forces/London_Dispersion_Forces). 2020.
- [11] *Electronic Structure of Atoms and Molecules* — chem.libretexts.org. [Accessed 04-Apr-2023]. 2023.
- [12] Paolo Giannozzi et al. “QUANTUM ESPRESSO: a modular and open-source software project for quantum simulations of materials”. In: *Journal of Physics: Condensed Matter* 21.39 (Sept. 2009), p. 395502. DOI: [10.1088/0953-8984/21/39/395502](https://doi.org/10.1088/0953-8984/21/39/395502).
- [13] *Graphene - Wikipedia* — en.wikipedia.org. [Accessed 06-May-2023].
- [14] David M. Hanson. *10.1: The Born-Oppenheimer Approximation* — chem.libretexts.org. [Accessed 05-Apr-2023]. 2022.
- [15] Philip J. Hasnip et al. “Density functional theory in the solid state”. In: *Philosophical Transactions of the Royal Society A: Mathematical, Physical and Engineering Sciences* 372.2011 (Mar. 2014), p. 20130270. DOI: [10.1098/rsta.2013.0270](https://doi.org/10.1098/rsta.2013.0270).
- [16] P. Hohenberg and W. Kohn. “Inhomogeneous Electron Gas”. In: *Physical Review* 136.3B (Nov. 1964), B864–B871. DOI: [10.1103/physrev.136.b864](https://doi.org/10.1103/physrev.136.b864).
- [17] Yuli Huang et al. “Bi-layer Graphene: Structure, Properties, Preparation and Prospects”. In: *Current Graphene Science* 2.2 (Jan. 2019), pp. 97–105. DOI: [10.2174/2452273202666181031120115](https://doi.org/10.2174/2452273202666181031120115). URL: <https://doi.org/10.2174/2452273202666181031120115>.
- [18] Dr. Sebastian Huber. *Correlations and flat bands* — cmt-qo.phys.ethz.ch. [Accessed 11-Apr-2023].

- [19] Anubhav Jain et al. “Commentary: The Materials Project: A materials genome approach to accelerating materials innovation”. In: *APL Materials* 1.1 (July 2013), p. 011002. DOI: [10.1063/1.4812323](https://doi.org/10.1063/1.4812323). URL: <https://doi.org/10.1063/1.4812323>.
- [20] Tilas Kabengele. *A Study of Ultra-Low Friction in Two-Dimensional Materials using Density-Functional Theory* — dalspace.library.dal.ca. <https://dalspace.library.dal.ca/handle/10222/80674>. [Accessed 06-Apr-2023]. 2021.
- [21] Tilas Kabengele. *Github - tilaskabengele/BiCrystal: BiCrystal is a Python 3 program that builds incommensurate unit cells of bilayer materials.* — github.com. <https://github.com/tilaskabengele/BiCrystal>. [Accessed 08-Apr-2023]. 2020.
- [22] Charles Kittel. *Introduction to solid state physics*. en. 8th ed. Nashville, TN: John Wiley & Sons, Oct. 2004.
- [23] Kristjan Haule. *Density Functional Theory*. Rutgers University. 2009.
- [24] *manifesto - Quantum Espresso* — quantum-espresso.org. <https://www.quantum-espresso.org/manifesto/>. [Accessed 08-Apr-2023]. 2022.
- [25] C. Fiolhais F. Nogueira M. Marques. *A Primer in Density Functional Theory*. Germany: Springer, 2003.
- [26] Anna Helena Mazurek, Łukasz Szeleszczuk, and Dariusz Maciej Pisklak. “Periodic DFT Calculations—Review of Applications in the Pharmaceutical Sciences”. In: *Pharmaceutics* 12.5 (May 2020), p. 415. DOI: [10.3390/pharmaceutics12050415](https://doi.org/10.3390/pharmaceutics12050415). URL: <https://doi.org/10.3390/pharmaceutics12050415>.
- [27] Ahmed Missaoui et al. “Numerical analysis of electronic conductivity in graphene with resonant adsorbates: comparison of monolayer and Bernal bilayer”. In: *The European Physical Journal B* 90 (Jan. 2017). DOI: [10.1140/epjb/e2017-70664-0](https://doi.org/10.1140/epjb/e2017-70664-0).
- [28] Ahmed Missaoui et al. “Numerical analysis of electronic conductivity in graphene with resonant adsorbates: comparison of monolayer and Bernal bilayer”. In: *The European Physical Journal B* 90.4 (Apr. 2017). DOI: [10.1140/epjb/e2017-70664-0](https://doi.org/10.1140/epjb/e2017-70664-0). URL: <https://doi.org/10.1140/epjb/e2017-70664-0>.
- [29] *Moire Superlattice* — everettyou.github.io. <https://everettyou.github.io/2018/05/21/Moire.html>. [Accessed 14-Apr-2023].

- [30] E. Suárez Morell et al. “Electronic properties of twisted trilayer graphene”. In: *Physical Review B* 87.12 (Mar. 2013). DOI: [10.1103/physrevb.87.125414](https://doi.org/10.1103/physrevb.87.125414). URL: <https://doi.org/10.1103/physrevb.87.125414>.
- [31] Tanja van Mourik, Michael Bühl, and Marie-Pierre Gaigeot. “Density functional theory across chemistry, physics and biology”. In: *Philosophical Transactions of the Royal Society A: Mathematical, Physical and Engineering Sciences* 372.2011 (Mar. 2014), p. 20120488. DOI: [10.1098/rsta.2012.0488](https://doi.org/10.1098/rsta.2012.0488). URL: <https://doi.org/10.1098%2Frsta.2012.0488>.
- [32] Jeong Min Park et al. “Tunable strongly coupled superconductivity in magic-angle twisted trilayer graphene”. In: *Nature* 590.7845 (Feb. 2021), pp. 249–255. DOI: [10.1038/s41586-021-03192-0](https://doi.org/10.1038/s41586-021-03192-0). URL: <https://doi.org/10.1038/s41586-021-03192-0>.
- [33] Steven H. Simon. *The Oxford Solid State Basics / Steven H. Simon.* eng. First edition. Oxford: Oxford University Press, 2013. ISBN: 9780191502101.
- [34] *The Many-Body Schrödinger Equation.* <http://www.tcm.phy.cam.ac.uk/~mds21/thesis/node12.html>. [Accessed 20-Dec-2022].
- [35] Johan Tidholm. *Lattice dynamics : From fundamental research to practical applications.* Dec. 2020. ISBN: 9789179297596. DOI: [10.3384/diss.diva-170800](https://doi.org/10.3384/diss.diva-170800).
- [36] *Valley ferromagnetism and superconductivity in magic-angle trilayer graphene — arxiv.org.* <https://arxiv.org/abs/2209.12964>. [Accessed 13-May-2023].
- [37] Johannes Voss. *Exchange-correlation Functionals — Johannes Voss — stanford.edu.* <https://stanford.edu/~vossj/slac/project/xc-functionals/>. [Accessed 20-Dec-2022].
- [38] *What Is Density Functional Theory and How Does It Work? — Synopsys — synopsys.com.* [Accessed 20-Dec-2022].
- [39] Chengyong Zhong et al. “Coexistence of flat bands and Dirac bands in a carbon-Kagome-lattice family”. In: *Carbon* 99 (2016), pp. 65–70. ISSN: 0008-6223. DOI: <https://doi.org/10.1016/j.carbon.2015.11.073>. URL: <https://www.sciencedirect.com/science/article/pii/S0008622315304814>.

Appendix

Appendix A: TriCrystal Repository

TriCrystal is a Python program that builds commensurate and incommensurate crystal structures of twisted trilayer graphene. The current version reads CIF files and writes the new structure to a Quantum Espresso input file.

Github repository: <https://github.com/anvibhagavathula/TriCrystal>